# Oil & Natural Gas Technology

**DOE Award No.: DE-FE0013531**

## Quarterly Research Performance
**Progress Report (Period ending 9/30/2015)**

## Assessing the response of methane hydrates to environmental change at the Svalbard continental margin
**Project Period (11/1/2013 to 10/31/2016)**


Submitted by:
Marta E. Torres

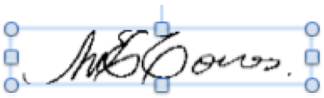

Oregon State University
DUNS #: 053599908
104 COAS Admin. Bldg.
Corvallis, OR 97331-5503
e-mail: mtorres@coas.oregonstate.edu
Phone number: (541) 737-2902


Prepared for:
United States Department of Energy
National Energy Technology Laboratory

**Office of Fossil Energy**

## EXECUTIVE SUMMARY

In November 2013, Oregon State University initiated the project entitled: **Assessing the response of methane hydrates to environmental change at the Svalbard continental margin**. In this project, we will take advantage of a unique opportunity to collect samples from the Svalbard continental margin. The overall objective of this research is to constrain the biogeochemical response of the gas hydrate system on the Svalbard margin to environmental change. Because of a delay in the planned expedition, we reconfigured the program based on discussions with NETL program managers and submitted a revised SOPO. In the new plan, we will collect samples in two expeditions, the first of which happened Oct 7-21, 2014. We were able to also join an expedition to the area onboard the RV Helmer Hanssen during May15-29, 2015 and another one onboard the RV Heincke August-September 2015

## PROGRESS, RESULTS, AND DISCUSSION

1. Expedition(s) update: We participated in the post cruise meeting for CAGE15-02 expedition in Tromso, Norway, 21-22 August, 2015. An article summarizing these results was submitted to Fire in the Ice on 09/02/15 (attached). Title: First report of near-surface gas hydrate, carbonate crusts and chemosynthetic organisms on a Vestnesa Ridge pockmark. Authors: G. Panieri, D. J. Fornari, P. Serov, E. K. Åström, A. Plaza-Faverola, J. Mienert, M. E. Torres, and the CAGE scientific team. In this article we document the deployment of a towed vehicle equipped with a high-resolution camera and multicore capabilities during the CAGE15-02 expedition. Our observation of a pervasive thin hydrate pavement, carbonate crusts and bacterial mats on surface sediments of two pockmarks along the Vestnesa Ridge, at approximately 79°N latitude adds to our understanding of gas hydrate dynamics and methane release to the Arctic ocean, which may impact carbon budgets and cycles, ocean acidification, and benthic community survival. In addition to this expedition, we also participated in another cruise onboard the RV Heinke in August-September 2015, which was focused on collecting water column samples
2. Water column technique. We submitted a manuscript to Limnology and Oceanography Methods on 09/15/15 describing the technique developed in this project for analyses of discrete water samples (attached). Title: Rapid analysis of methane concentration in water samples using headspace equilibration and Off-Axis Integrated Cavity Output Spectroscopy (ICOS). Authors: P. Geprägs, M. E. Torres, T. Fleischmann, S. Mau, T. Pape, G. Bohrmann. In this paper we describe a novel and simple method for the analysis of discrete water samples, which extends the applicability of this technology also to deep-water samples. We document the suitability of the approach to both marine and fresh water systems. Samples are collected in large plastic syringes; headspace is generated using methane-free air and is analyzed with a Greenhouse Gas Analyzer (GGA, Los Gatos Research) after equilibration. Measuring one sample, including headspace addition, injection into the GGA and analysis of the sample, takes only 5–10 min. Methane concentrations ranging from 1.5–65000 nM are detectable with a precision better than 2.5%, thus allowing for measurements that range from typical seawater concentrations to the extremely high abundances encountered at methane seeps or in peat channels. This ability to generate data in the field is highly advantageous in refining sampling strategies. The

approach described here enables fast and accurate measurements of methane in the field, uses low cost and reusable materials, and does not require chemicals for sample preservation.

3. Water column results. We conducted extensive sampling campaign of the water column along the entire Barents Sea-Svalbard margin in August-September 2015, including the shelf regions, to document the significance of methane release at the upper limit of gas hydrate stability relative to additional sources on the shelf. Water and air samples collected during two RV Heinke expeditions indicate that the methane released in the slope does not contribute to the atmospheric input, however the shelf regions do. In addition extensive hydroacoustic surveys along the entire edge of has hydrate stability do not show any methane discharge expect for the well-studied region offshore Prins Karl Foreland.
4. Geochemistry: We continue the analyses from the CAGE 15-2 Expedition, which include carbon isotopes in the DIC, oxygen and hydrogen isotopes in water and nutrient concentrations. Preliminary data from a series of cores recovered at on the fan of Storfjordrenna, west Barents Sea from a location where gas hydrate was recovered as shallow as 0.82 mbsf indicate that the increase in methane flux inferred sulfate profile, may be linked to an enhanced gas hydrate dissociation in this area. Ongoing studies are aimed at testing this postulate, with the aim to bridge the gap between hydroacoustic flare detection in the water column and the mapping of hydrate reservoir at depth, and provide additional clues to unravel the complex interactions among ice, ocean, microbiology and climate and their sensitivity to both natural and anthropogenic change in Arctic regions. We expect to submit a manuscript n this observations early 2016.
5. Modeling- A second manuscript was submitted to Journal of Transport in Porous Media on 06/08/2015, as a companion paper to the one submitted to this journal on 06/08/2015. Title " Methane hydrate formation under conditions of variable salinity II. Time-stepping variants and sensitivity of reduced numerical model." Authors: M. Peszynska, F. P Medina, W-Hong, M.E. Torres. In this paper we consider a reduced model of methane hydrate formation in variable salinity conditions presented in a companion paper, and give details on discretization and three time-stepping variants: Implicit, Semi-implicit, and Sequential. We compare their accuracy and efficiency depending on the spatial and temporal discretization parameters. We also study sensitivity of the model to the simulation parameters and in particular to the reduced phase equilibria model. (Keywords methane hydrate formation; numerical discretization; implicit and non-implicit timestepping; model sensitivity and convergence; multiphase multicomponent model).

**PROBLEMS OR DELAYS**

No new problems since the set-back last year when the planned expedition in the R/V M.S. Merian got cancelled due to massive engine failure of the vessel. We completed our expedition plan to the area as documented in the revised project plan and added an additional cruise on the RV Hanssen in May 2015.

## PRODUCTS

- FITI article. An article summarizing these results was submitted to Fire in the Ice on 09/02/15. Title: First report of near-surface gas hydrate, carbonate crusts and chemosynthetic organisms on a Vestnesa Ridge pockmark.
- Manuscript to Limnology and Oceanography Methods submitted 09/15/15 describing the technique developed in this project for analyses of discrete water samples. Title: Rapid analysis of methane concentration in water samples using headspace equilibration and Off-Axis Integrated Cavity Output Spectroscopy (ICOS).
- Second manuscript submitted to the Journal of Transport in Porous Media on 06/08/2015, as a companion paper to the one submitted to this journal on 06/08/2015. Title " Methane hydrate formation under conditions of variable salinity II. Time-stepping variants and sensitivity of reduced numerical model".

# First report of near-surface gas hydrate, carbonate crusts and chemosynthetic organisms on a Vestnesa Ridge pockmark

Giuliana Panieri, Daniel J. Fornari, Pavel Serov, Emmelie K. Åström, Andrea Plaza-Faverola, Jürgen Mienert, Marta E. Torres, and the CAGE scientific team*.

CAGE - Centre for Arctic Gas Hydrate, Environment and Climate - UiT The Arctic University of Norway, Woods Hole Oceanographic Institution, Oregon State University

Most of the deep sea floor on the Artic Ocean is characterized by a rather featureless muddy or ice-drafted debris sediment. During the CAGE15-2 cruise in May 2015, we deployed a towed vehicle equipped with a high-resolution camera and multicore capabilities. Our observation of a pervasive thin hydrate pavement, carbonate crusts and bacterial mats on surface sediments of two pockmarks along the Vestnesa Ridge, at approximately 79$^{o}$N latitude adds to our understanding of gas hydrate dynamics and methane release to the Arctic ocean, which may impact carbon budgets and cycles, ocean acidification, and benthic community survival.

## Vestnesa gas hydrate Ridge

Vestnesa Ridge, is a ~100 km long and ~ 100 m high, SE-NW oriented elongate feature comprising largely drifted sediment in the Fram Strait, north of the Molloy Transform Fault in water depths of ~1200 m (Figure 1). It is characterized by intensive seabed faulting and rifting, and by 400 to 600 m wide pockmarks that lie above sub-seabed acoustic blanking zones indicative of gas transport. The two features described here are active gas release systems, based on repeated hydroacoustic flare mapping. The flares nearly reach the sea surface (Figure 1b). Gas analyses indicate both biogenic and thermogenic hydrocarbon sources with migration pathways likely controlled by a tectonically induced reactivation of fracture networks.

## Methods

The towed vehicle, based on the Woods Hole Oceanographic Institution (WHOI) MISO TowCam deep-sea imaging system, is equipped with a deep-sea digital camera and CTD real-time system that provides both altimetric and depth data (http://www.whoi.edu/main/instruments/miso). The UiT multicorer system (TC-MC) allowed for collection of six 60 cm-long visually-guided cores. Deployment of the instrument along the six survey lines shown in Figure 1a was guided by hydroaustic and bathymetry data.

## Highlights

Acoustic flares indicative of active gas releases are aligned along the eastern edge of the Vestnesa gas hydrate ridge a , where 4D seismic data indicate rising gas within the sediment. Repeated camera surveys showed that the sea floor outside the pockmark area is soft muddy sediment extensively bioturbated by fauna consisting primarily of Ophiurioids and Polychaete tubes. Within the pockmark, gas seepages are highly localized, and small patches of bacterial mats 3 to 4 meters in diameter occur. Individual white bacterial mats are ~20 cm in length, typically surrounded by black sediment, which in the TC-MCs cores was identified as containing abundant iron sulfide minerals. Large carbonate blocks (Figure 2b) and outcrops are common in the seep areas and range from 10 cm to more than 2 meters in length; in some cases they rise up to 3 meters above the seafloor. The blocks are colonized by abundant epifauna, as they provide a hard bottom substrate for sessile benthic organisms and shelter for mobile megafauna.

Cracks in the seafloor expose a thin crust (ca. 2-3 cm) of surface sediment cemented by gas hydrate layers (Figure 1c). The pavement is prevalent in seep areas and is colonized by dense mats of tube-dwelling polychaetes (Figure 2a), as confirmed by benthic sampling. Multicore samples from these areas also reveal the presence of abundant frenulating tubeworms, belonging to the family Siboglinidae, known to live in an obligate mutualistic association with chemosynthetic bacteria.

Analyses of the uppermost sediment yield a methane concentration of 5 mM. Saturation with respect to gas hydrate is 59.7 mM. Methane values below saturation reflect extensive degassing of the core as evidenced by intense bubbling observed for ~30 minutes in all of the 5 cores recovered from this site. Marker CAGE 888 was deployed to allow for future time series investigations using seafloor observatories for methane seepage record at this site.

**Impacts and Consequences**

Seepage at the CAGE 888 pockmark is highly localized, indicative of focused flow of methane. Our observations are consistent with seismic data (Fig. 1c) that revealed discrete, fine scale (<10 m), methane migration pathways, usually capped by strong seafloor reflections suggestive of the presence of authigenic carbonate.

It is well know that areas where gas hydrate outcrops at the seafloor as for examp,e on Hydrate Ridge, Gulf of Mexico, and elsewhere show large thickets of Lamellibrachia and abundant *Vesicomyidae* bivalves. In contrast, the various camera surveys and benthic sampling in the Vestnesa pockmark area revealed a seafloor with small scale heterogeneity, rich and diverse microbiological communities and small tubeworms assemblages, but not the expected colonies of chemosynthetic organisms. Our observations are consistent with other active gas seeps and plume area along western Svalbard margin and in the Barents Sea.

The occurrence of gas hydrate in Vestnesa, particularly in the near surface sediments described here, but also as previously documented at ~2m below seafloor attests to the presence and current abundant supply of methane to the seafloor. This methane flux and the hydrogen sulfide generated by anaerobic oxidation of methane, sustain the bacterial communities observed in our camera surveys. The question still remains as to why, at present, there are no communities of large chemosynthetic associated taxa, rather the seepage here is associated with discrete patches of bacterial mats and small tubeworms assemblages.

Our new observation of near surface gas hydrate pavements within the Vestnesa pockmarks, and their association with methane plumes in the water column suggest the presence of similar near surface deposits along the Arctic margin, where

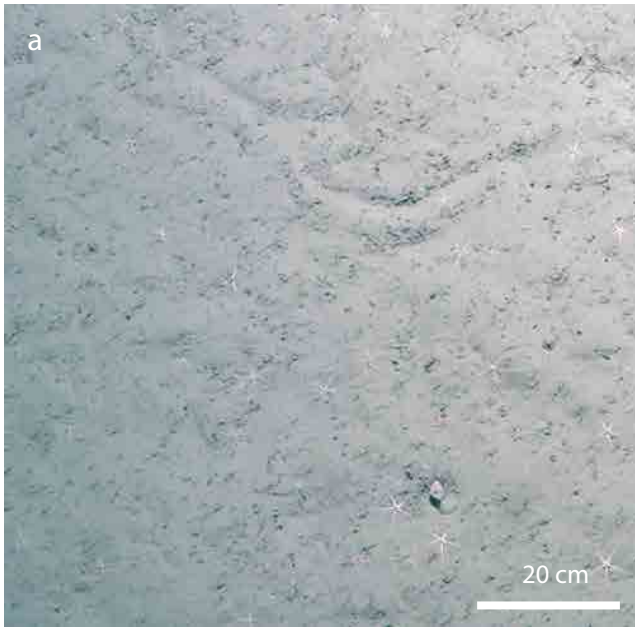
a
20 cm

b
20 cm

c

d
2 cm

# Rapid analysis of methane concentration in water samples using headspace equilibration and Off-Axis Integrated Cavity Output Spectroscopy (ICOS)

Patrizia Geprägs[1,*], Marta E. Torres[2], Timo Fleischmann[1], Susan Mau[1], Thomas Pape[1], Gerhard Bohrmann[1]

[1]MARUM – Center for Marine Environmental Sciences, Department of Geosciences, University of Bremen, Klagenfurter Str., 28359 Bremen, Germany

[2]School of Oceanic and Atmospheric Sciences, Oregon State University, 104 Ocean Admin Building, Corvallis, OR 97331-5503, United States

*corresponding author. E-mail: pgepraegs@marum.de; tel: +49 421 218 65055

Keywords: dissolved methane, headspace equilibration, Integrated Cavity Output Spectroscopy, discrete sampling, deep sea samples, greenhouse gases, fast and accurate, Vacuum Extraction

## Abstract

Laser-based instrumentation utilizing the off-axis integrated output spectroscopy (ICOS) technology has become increasingly popular for the continuous measurement of methane in air and surface seawater. Here we describe a novel and simple method for the analysis of discrete water samples, which extends the applicability of this technology also to deep-water samples. We document the suitability of the approach to both marine and fresh water systems. Samples are collected in large plastic syringes; headspace is generated using methane-free air and is analyzed with a Greenhouse Gas Analyzer (GGA, Los Gatos Research) after equilibration. Measuring one sample, including headspace addition, injection into the GGA and analysis of the sample, takes only 5–10 min. Methane concentrations ranging from 1.5–65000 nM are detectable with a precision better than 2.5%, thus allowing for measurements that range from typical seawater concentrations to the extremely high abundances encountered at methane seeps or in peat channels. This ability to generate data in the field is highly advantageous in refining sampling strategies. The approach described here enables fast and accurate measurements of methane in the field, uses low cost and reusable materials, and does not require chemicals for sample preservation.


## Introduction

Methane is an important greenhouse gas, whose atmospheric concentration has increased by a factor of 2.5 since preindustrial times (IPCC 2013). Because the warming potential of methane is 21 times that of carbon dioxide (IPCC 2007) it plays an important role in the current global warming (Badr et al. 1991). Even though the ocean source is thought to have only a small impact on the global methane budget, there is a lack of data to fully quantify this input source, such that its contribution, especially from shallow regions may be underestimated. It is possible that the ocean source term has been increasing due to ocean warming and release from either gas hydrate or permafrost (Bange 2006).

Methane generated in marine sediments can accumulate below the seafloor and at some locations it discharges at cold seeps, either dissolved in fluids or, in the case of over-saturation, in the form of methane bubbles. In addition, conspicuous maxima in dissolved methane have been documented in oxic water layers, revealing production under oxic conditions in the water column (Traganza et al. 1979; Holmes et al. 2000; Damm et al. 2009). There is clearly a need to monitor methane concentrations in the water column, if we are going to fully constrain its role in the global carbon cycle and its potential contribution to the atmosphere. The pressing need for methane surveys is also evidenced in recent publications describing analytical approaches (e.g. Gülzow et al. 2011; Arévalo-Martínez et al. 2013; Magen et al. 2014; Li et al. 2015). Magen et al. (2014) described collection and preservation of water samples for subsequent measurement of methane in the headspace using gas chromatography, up to 3 months after collection. With the advent of off-axis integrated cavity output spectroscopy (ICOS), new instrumentation became commercially available for the continuous monitoring of greenhouse gases (methane and carbon dioxide) at atmospheric levels with high precision and accuracy (Baer et al. 2002; Berman et al. 2012). This analytical breakthrough was expanded to continuously monitor $CH_4$ and $CO_2$ in surface seawater samples by use of an equilibrator system (Schmale et al. 2010; Gülzow et al. 2011; Arévalo-Martínez et al. 2013; Li et al. 2015). Thereby, the water enters equilibrators where a constant volume of air is circulated through the water and equilibrates with the water phase. The air is then dried and transported to the analyzer and measured via ICOS (Gülzow et al. 2011). These two approaches combined, atmosphere and surface seawater analyses, allow for monitoring processes at the seawater-atmosphere interface at high resolution. However, not all of the methane entering the water column reaches the atmosphere. When methane is emitted as bubbles on the seafloor, a fraction of the gas dissolves during transit through the water column depending on release depth, bubble volume and the buoyancy of the plume (e.g. Greinert & McGinnis 2009). Bubble dissolution creates patches of dissolved methane (Clark

et al. 2003), which in cases where methane emissions are persistent and of sufficient magnitude can form large continuous plumes. Only if this dissolved methane is transported to the mixed layer, it can be transferred to the atmosphere via sea-air gas exchange; the amount depends especially on wind speed (e.g. Mau et al. 2007). Furthermore, studies have shown that the methane within bubbles can be replaced by other gases via exchange processes during bubble ascent through the water column (e.g. McGinnis et al. 2006) . In addition, microbial consumption of $CH_4$ restricts its release into the atmosphere (Reeburgh 2007), and aerobic oxidation of methane may contribute to ocean acidification (e.g. Biastoch et al. 2011). To fully constrain the methane budgets, sources to and microbial consumption in seawater, it is important to generate concentration profiles of dissolved methane throughout the entire water column. Here, we describe a simple and rapid method to measure methane in discrete water samples using ICOS technology, which allows for results to be generated in the field shortly after sampling. Furthermore, as this instrumentation can also generate air and surface seawater measurements with minimal modification, a complete depiction of methane in ocean/atmospheric system can be obtained.

## Material and procedures

### Material

Analyses by GGA require a total gas volume of 140 ml. Therefore, we used 140 ml plastic syringes with a rubber plunger head (Monoject$^{TM}$) for sample collection at sea, where these syringes were filled directly from Niskin bottles. Small water bodies on land were sampled directly from shore. The syringes were each attached to a one-way valve to close them and we used a 22-gauge needle (e.g. Hamilton SN 7751-13) for sample processing.

Methane free synthetic air (known as 'Zero Air') is required for measurement procedure and various gas standards for calibration of the ICOS. Zero Air is available from Air Liquide (Germany) as ALPHAGAZ_1 in 200L or 50 L tanks or as N12, in small (12L) pressured portable canisters. We used three methane standards with different concentrations for the calibration of the analytical instrument (1, 10 and 100 ppm). The 1 ppm and 10 ppm standards were supplied by Air Liquide as custom-made products (Chrystal gases), these have to be purchased in larger quantities (min. 10L) but can be requested in small canisters

Analyses were done by off-axis integrated cavity output spectroscopy (ICOS), using the Greenhouse Gas Analyzer (GGA- 'Enhanced Performance' with 'Syringe Injection Mode') from Los Gatos Research (LGR), California. The instrument uses conventional Laser Absorption Spectroscopy, where the absorption of the infrared laser beam directed through the sample is used to calculate the mole fraction of methane in the gas. The use of high reflectivity mirrors in the absorption cell enlarges the optical path length by thousands of meters and thus the measured IR absorption is significantly enhanced (Baer et al. 2002). A small vacuum pump and the required tubing are included in this set up, additional septa for the injection port have to be ordered separately from LGR.

**Procedure**

At sea, water samples are taken with Niskin bottles, either during hydrocasts or using a remotely operated vehicle. Immediately upon recovery, each Niskin bottle is sampled by filling three 140-ml syringes outfitted with a valve. Tygon tubing were used to fill the syringes to avoid potential water degassing induced by turbulence during sampling. The syringes were flushed and filled with exactly 100 ml of seawater without any air bubbles. Two syringes were used for the analysis, and the remaining one was saved as a spare.

For analyses of methane in water streams or ponds, samples can be collected directly on 140-mL syringes, and transported to the lab for immediate analyses. To test the reproducibility of

the method in fresh water, we collected up to 10 L of surface water from a peat channel in Bremen, Germany. Subsamples in 140-ml plastic syringes were taken within 10 minutes of collection.

After water collection either from Niskin or surface waters, the syringes were left to equilibrate to room temperature for at least 30 minutes and room temperature and ambient pressure were noted at the beginning of the analytical run. In some cases the samples are very cold around 1°C, to avoid a long equilibration time the sample temperature can be taken shortly after the injection. To generate a gas headspace within the syringe 40 ml of Zero Air were drawn from a 200 L gas tank outfitted with a septum port through a needle attached to the syringes. Potential overpressure was released, the valve was closed and the needle was removed. The procedure was repeated for the second syringe. Both syringes were shaken vigorously for over 1.5 minutes to allow for equilibration between water and headspace (Magen et al. 2014). To minimize the risk of water injection into the GGA instrument chamber the 40 ml headspace gas each from both syringes were collected in a gas tight 100 ml glass syringe via a Luer Lock adapter and the combined gas volume of 80 ml was injected in the GGA. This was followed immediately by 60 ml injection of Zero Air, as needed to reach the required volume of 140 ml in the instrument chamber of the GGA. Each analytical run took 5 minutes, during which more than 100 readings were acquired.

## Calculations

Each GGA run collects around 104 measurements, which are stored in a text file that can be downloaded directly from the instrument. The GGA calculates methane concentrations based on its internal calibration. Because water vapor interferes with the $CH_4$ concentration by diluting the mixing ratio in air and by broadening the spectroscopic absorption lines (Rella et al. 2013; Welp et al. 2013) the water vapor content of the gas sample is automatically

137 determined and methane concentrations are corrected accordingly and reported as dry
138 methane. To minimize potential errors caused by shifts in the internal calibration of the
139 instrument we ran calibration curves at the beginning of each day, where 30–40 samples were
140 analyzed (see assessment section). A small application with web-installer named TICOSES
141 using the MATLAB Compiler Runtime environment, extracts the measured data (methane,
142 water vapor, carbon dioxide) and relevant parameters (gas pressure, gas temperature,
143 instrument ambient temperature, ringdown time of both lasers) as well as derived variables
144 (methane dry, carbon dioxide dry). Further calculations like the mean concentration and the
145 standard deviation are also performed by the software, stored in two data tables. TICOSES
146 with MATLAB Runtime web-installer is given in the supplemental material. Calculation of
147 the dissolved methane concentration in the samples used the corrected dry methane values,
148 the atmospheric ambient pressure, the water sample volume and the volume of injected gas.
149 Calculations are based on the headspace formulation detailed in Magen et al., (2014). Briefly:

150

151 $$n_{CH_4} = n_{CH_{4W}} + n_{CH_{4HS}} \quad (1)$$

152 $$[CH_4]_{GGA} = n_{CH_4}/V_W \quad (2)$$

153

154 where $nCH_4$ is the sum of moles of methane in the water and the headspace gas. To calculate
155 the methane concentration in the water sample after equilibration, the atmospheric ambient
156 pressure and the Bunsen coefficient were used, which required knowledge of salinity and
157 temperature of the sample to define the solubility of methane (Yamamoto et al. 1976). The
158 methane concentration in the GGA ($[CH_4]_{GGA}$) was calculated using the volume of water in
159 the syringes ($V_W$). Because of the need to dilute the headspace with a volume of Zero Air in

160 the instrument chamber, the final methane concentration is corrected with the dimensionless
161 dilution factor, such that the methane concentration in the sample ($[CH_4]_{smp}$) is given by

162

163 $$[CH_4]_{smp} = [CH_4]_{GGA} \times 140/V_{HS} \quad (3)$$

164

165 where $V_{HS}$ is the volume (in ml) of headspace gas injected and 140 is the total gas volume in
166 ml injected in the GGA chamber.

167

168 # Assessment

169 ## Analytical range

170 Supplier's specifications indicate a linear instrument response of the GGA in concentrations
171 ranging from 0.01 to 100 ppm. The method described here takes advantage of this broad range
172 to measure dissolved methane in samples over an extremely wide concentration range (1.5 to
173 65,000 nM), with minimal modifications to the sample protocol. This allowed us to analyze
174 water samples in the water column directly above methane seep areas, where concentrations
175 range by 3 orders of magnitude within one hydrocast. The only constrain to the dynamic
176 range is that the instrument requires 140 ml of gas for each run. The protocol described above
177 (80 ml headspace diluted with 40 ml of Zero Air) is optimal for typical low seawater
178 concentrations, which have methane concentrations of 2–5 nM (e.g. Bange et al. 1994;
179 Tsurushima et al. 1996; Valentine 2011). For samples above 3,200 nM methane, different
180 headspace to Zero Air ratios can be used. For example, for very high methane concentrations
181 (>5µM), we injected 10 ml of headspace gas using a smaller glass syringe and 130 ml Zero

Air. If the volume of the water sample is reduced to 70 ml and 70 ml of headspace gas are added, a maximum of 65 µM methane can be detected.

**Instrument response**

The instrument precision, calculated as the relative standard deviation of 80 analytical runs is 0.067%. The linearity of the GGA response is shown in Figure 1. We used dilutions of three stock standards (1, 10 and 100 ppm methane) and generated calibration curves ranging from 0.07 to 100 ppm. For the lower concentration range (0.07–10 ppm) the GGA responded linearly with an $R^2$ of *0.9999* and a slope of 0.90. However, for concentrations exceeding 10 ppm, we used a second calibration curve, with a linear response $R^2 = 0.9992$, but with a different slope of 0.71, which could be due to using various standards. Our results show that the use of Zero Air to dilute headspace sample within the instrument chamber, followed by GGA analyses, yields data with precision better than 2.4% (Table1).

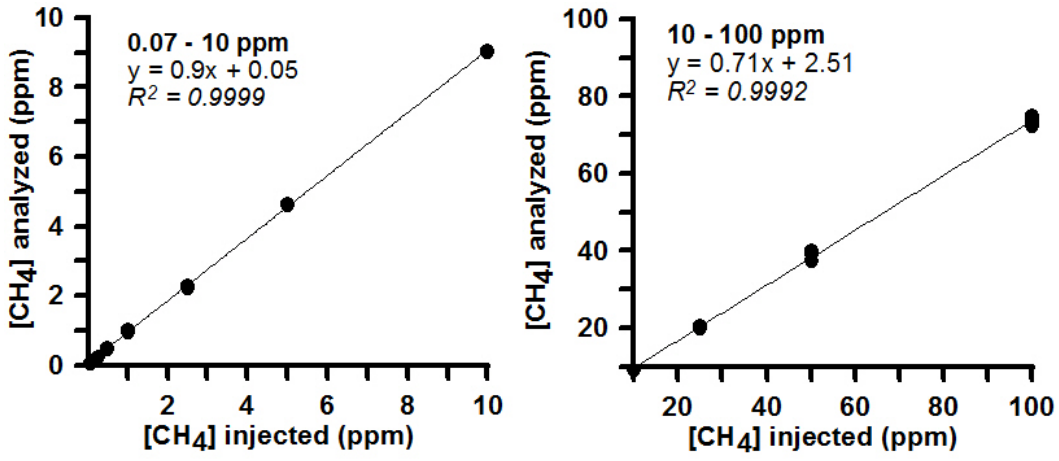


Figure 1: Response of GGA using dilutions of three (1, 10, 100 ppm) stock Air Liquid standards. The 100 ppm standard yields a different slope compared to the values obtained using the lower stock concentrations, therefore we chose two different calibration curves.

200 **Table 1**: Reproducibility of syringe injections using a 1 ppm, 10 ppm and 100 ppm methane
201 standard gas and various mixing ratios with Zero Air, mixing ratio is represented in the
202 injected standard gas volume ($V_S$) and the volume of Zero Air ($V_{ZA}$). Precision was calculated
203 on the basis of standard deviation divided by the mean of each analyzed $CH_4$ concentration.

| **$CH_4$ injected [ppm]** | **$V_S$ [ml]** | **$V_{ZA}$ [ml]** | **Number of samples** | **$CH_4$ analyzed [ppm]** | **Precision [%]** |
|---|---|---|---|---|---|
| 0.07 | 10 | 130 | 6 | 0.07 | 2.34 |
| 0.25 | 35 | 105 | 6 | 0.24 | 1.22 |
| 0.5 | 70 | 70 | 10 | 0.49 | 1.78 |
| 1.0 | 140 | - | 28 | 0.97 | 1.42 |
| 2.5 | 35 | 105 | 7 | 2.26 | 1.15 |
| 5 | 70 | 70 | 8 | 4.63 | 0.38 |
| 10 | 140 | - | 17 | 9.06 | 0.14 |
| 25 | 35 | 105 | 8 | 20.42 | 1.54 |
| 50 | 70 | 70 | 13 | 39.38 | 1.79 |
| 100 | 140 | - | 41 | 73.57 | 0.90 |

204

205 **Limit of detection**

206 The limit of detection (LOD) was calculated after Currie (1968) using the formula:

207 $$LOD = 3.29 \times \sigma_{blank} \quad (4)$$

208 where $\sigma$ represents the standard deviation of blank injections, for which we use 140 ml of
209 Zero Air. The LOD obtained (n = 33) is 0.0068 ppm methane. This concentration is not
210 significantly different from the lowest threshold of the GGA, reported to be 0.01 ppm from
211 the supplier, and reflects potentially methane content of the Zero Air used. Therefore, there is
212 no need to use Zero Air of higher purity. The lowest methane concentration we analyzed in
213 seawater is ~2 nM; using 200 ml of seawater, an injection volume of 80 ml headspace gas and
214 60 ml Zero Air, yields $[CH_4]_{GGA} \geq 0.05$ ppm, and therefore, clearly is within the detection
215 range of the instrument.

216 **Precision of the Headspace-GGA technique**

217 We tested the reproducibility of our method in both fresh and seawater samples. Water from
218 the freshwater peat channel 'Am Fleet' (Bremen, Germany) was collected in large volumes
219 (~10 L) during the summers of 2014 and 2015, which were subsampled and analyzed
220 immediately after collection at the nearby University of Bremen. Repeated seawater
221 measurements were conducted onboard the research vessel RV METEOR using water
222 samples collected in the Gulf of Mexico above hydrocarbon seeps (Table 2). Repeated
223 analyses (n= 26) yield a precision <2.5%. Am Fleet in 2015, when various operators
224 conducted analyses during training with freshwater samples a precision of 2.1% was reached.
225 This is also reflecting the ease of use and reliability of the method.

226 **Table 2**: Precision reported as the mean of relative standard deviation of repeated methane
227 measurement using different methods, and samples with different salinities and concentration
228 ranges.

| Site | Salinity [psu] | Number of samples | Concentration range $CH_4$ [nM] | Precision [%] |
|---|---|---|---|---|
| Headspace - Greenhouse Gas Analyzer | | | | |
| Am Fleet '15 | 0 | 43 | 980–3200 | 2.10* |
| Gulf of Mexico | 35 | 18 | 4–82 | 2.50 |
| Gulf of Mexico | 35 | 8 | 111–243 | 2.39 |
| Vacuum Extraction - Gas Chromatography | | | | |
| Gulf of Mexico | 35 | 3 | 62–70 | 5.87 |
| Gulf of Mexico | 35 | 3 | 225–274 | 10.84 |

229 *various operators

230

231 **Sample storage**

232 This method was developed for rapid and accurate analysis of dissolved methane
233 concentrations in the field. The sampling described here, using plastic syringes, was deemed
234 accurate over minimum 2-hour time-series. Duplicates of samples were analyzed after 1,2, 14
235 and 20 hours, significant loss of methane in the plastic syringe of 20% was observed after 14
236 hours (Figure 2). We did not consider long-term storage as part of this study, since Magen et
237 al. (2014) have provided a detailed report of sample preservation with KOH and NaOH for
238 analyses up to one year after sample collection.

239 Because the instrument is small and requires no carrier gas, it is relatively easy to transport to
240 the field. Standards and Zero Air canisters are available for ease of transportation. If analyses
241 in the field cannot be achieved, headspace gas samples can be obtained with the new
242 technique described here and be stored in 100-ml glass bottles filled with saturated NaCl
243 solution, and transported to the lab for later analyses. Alternatively, water samples can be
244 collected in 200 ml glass vials equipped with a septum and preserved with NaOH for shore-
245 based gas extraction and GGA analyses.

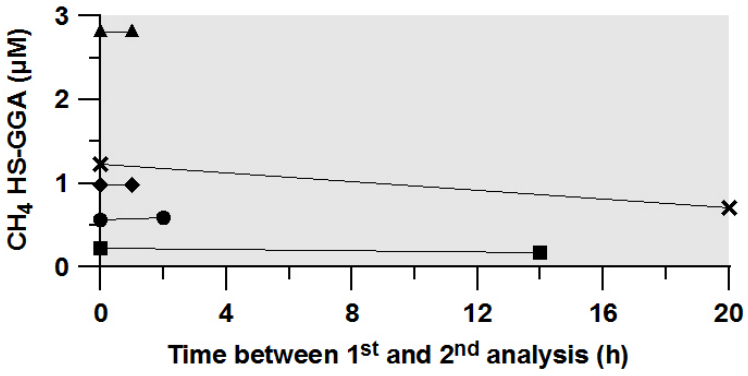


246

247 Figure 2: Repetition of samples using the HS-GGA method showing methane concentration
248 of duplicate samples analyzed after different time steps.

249 **Comparison with Vacuum Extraction method**

250 We took advantage of two research expedition onboard FS METEOR to compare our method
251 with the Vacuum Extraction method after Lammers and Suess (1994) modified after Rehder
252 et al. (1999) and Keir et al. (2005, 2009). This technique extracts gas compounds from water
253 using vacuum. Briefly, 700 to 750 mL of seawater are directly collected from Niskin bottles
254 into pre-evacuated ($1x10^{-3}$ mbar) 1L-glass bottles (Schott DURAN), which have a gas tight
255 closure. The gas dissolved in the sample is separated from the water by high-grade vacuum
256 extraction in the bottles. The extracted gas can be transferred with a gas-tight syringe through
257 a septum port in the extraction system into a 20 ml serum glass vial pre-filled with saturated
258 NaCl solution. These gas samples were analyzed for methane concentration with a gas

chromatograph using a Flame Ionization Detector and/or can be used for characterization of stable carbon isotope composition (Pape et al. 2010).

Drawbacks of this traditional method are securing vacuum and the necessity of more equipment for extraction of the gas. The potential for error using the vacuum extraction method is high because of the number of technical steps involved and the need to ascertain full vacuum of $1x10^{-3}$ mbar in the glass bottles, which was not always achieved or got lost over time as bottles leaked. We tested the reproducibility of the Vacuum Extraction method analyzed with the gas chromatograph (VE-GC) using triplicate samples, which yield precision values of 5 to 10% (Table 2). The vacuum technique also requires significantly more equipment (vacuum pumps, glass bottles, stop cocks, magnetic stirrer, glass valves and tubing etc.), that needs a lot of space and is partly quite expensive.

For the comparison with the HS-GGA method some water samples were analyzed with the VE-GC method, and shown as discrete grey symbols in Figure 3. In all cases, both methods yield the same trend, with partly indistinguishable variations given the large concentration ranges encountered. Interestingly, in some cases the concentration measured using the VE-GC method was lower than that detected with the HS-GGA, indicating incomplete extraction with the vacuum approach. But for background samples with concentrations <5nM, methane concentrations determined with the HS-GGA were constant between 1.1 and 1.9 nM whereby the values analyzed with the VE-GC approach revealed higher concentrations around 3.5 nM methane. The reason for higher values detected with the VE-GC method could be contamination with atmospheric air, e.g. due to a poor vacuum in the bottle.

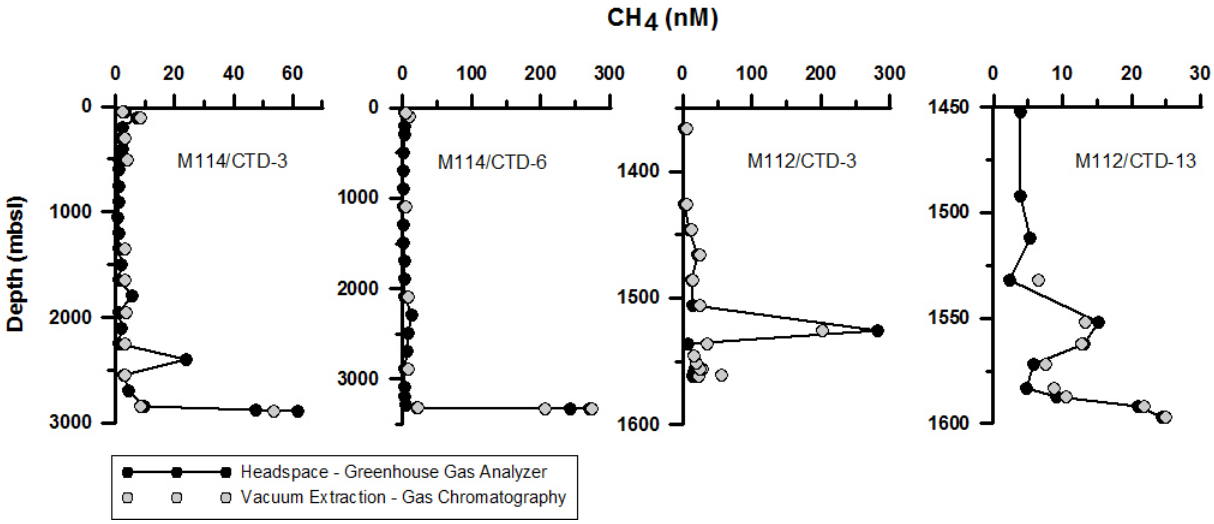


281

282 Figure 3: Vertical concentration profiles of dissolved methane in the water column using the
283 HS-GGA method (black symbols) and the VE-GC (grey symbols) obtained for ship stations
284 performed during cruise M112 and M114.

285

286 **Field results**

287 The field results presented here were compiled from different settings and are supposed to
288 provide examples of the usage of ICOS. First we cover field data of the marine realm and then
289 freshwater settings.

290 As already mentioned above, during expeditions, M112 and M114 with RV METEOR
291 (Bohrmann et al. 2014), water samples were collected for methane analyses using the HS-
292 GGA approach to test the handling of the equipment. Both cruises had the objective to
293 characterize methane released from the seafloor. Therefore, sampling was guided by
294 observation of gas flares during hydroacoustic surveys, such that targeted hydrocasts were
295 conducted as close as possible to the seepage sites.

296 The majority of the analyses were conducted with the HS-GGA method, because of its' large
297 analytical range and ease of use. Furthermore, the HS-GGA method was found to be more

298 reliable due to a better reproducibility and an entire hydrocast of 24 samples was analyzed in
299 3–4 hours, including calibration curve and a few duplicate runs.

300 Examples from four hydrocasts are shown in Figure 3. High methane concentrations (30–300
301 nM) were found near the seafloor. Plumes in the water column were also detected, with
302 maximum concentrations reaching over 250 nM in the vicinity of mud volcanoes in the
303 Mediterranean. Details of sources and patterns observed are discussed elsewhere (P. Gepraegs
304 unpubl.).

305 Freshwater samples from the channel 'Am Fleet' were analyzed using the HS-GGA technique
306 in September 2014 and July 2015 (Figure 4) to test the reproducibility and to investigate
307 potential correlation between environmental conditions e.g. rain fall and methane in the
308 system. In this case the methane concentrations were higher, thus, only one syringe filled with
309 100 ml water was used for the analysis and 40 ml headspace were injected diluted with 100
310 ml Zero Air. In 2015, at least 5 sample repetitions were taken, and precision was always better
311 than 2.5%, error bars are within the symbol and therefore, not displayed in Figure 4. The
312 detected concentrations varied between 0.2 and 3.2 µM methane. The vertical bars in Figure 4
313 indicate the air temperature and precipitation height on each day representing environmental
314 conditions during sampling (Deutscher Wetterdienst, http://www.dwd.de, July 2015). No
315 correlation between rainfall and temperature could be observed. Discussion of reasons for
316 observable change in methane concentration and variability is out of the scope of this
317 publication.

318 An advantage of using the GGA is that it allows for simple way to also obtain air methane
319 concentrations (Baer et al. 2002; Berman et al. 2012). Our measurements of methane in air
320 samples collected in Bremen during our field experiments, yield concentrations ranging from
321 0.08 to 0.09 µM, indicating the extreme methane super saturation of the peat channels, which
322 undoubtedly constitute a significant methane source to the atmosphere.

323

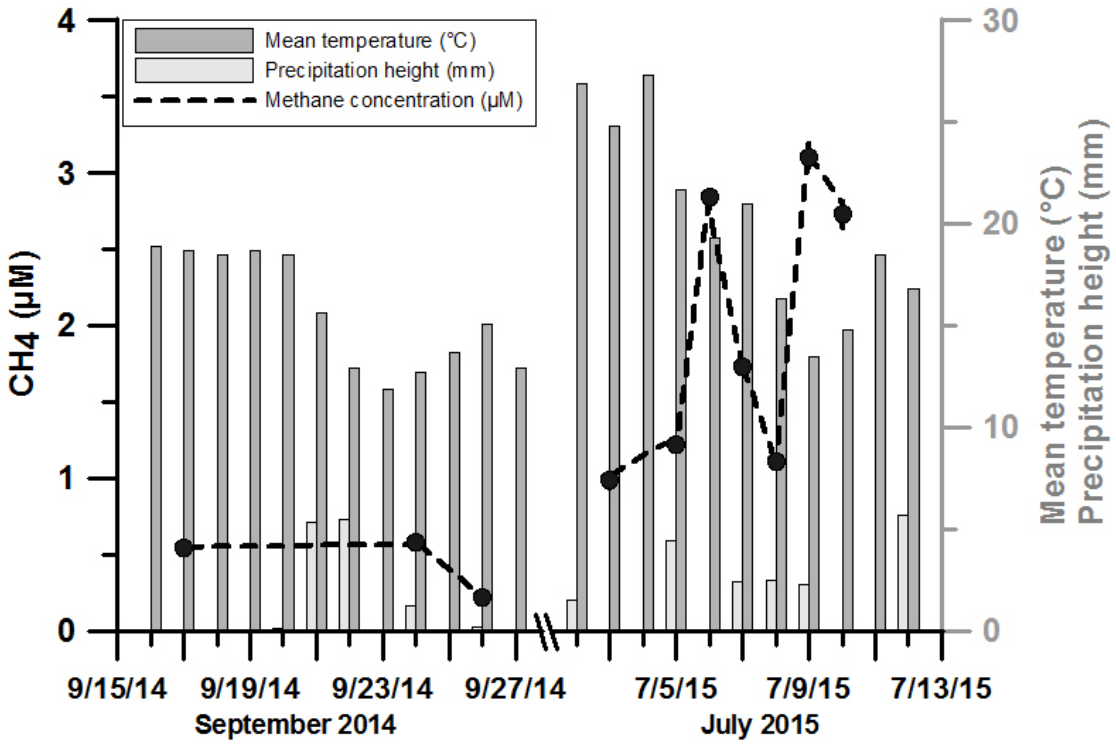


324

325 Figure 3: Methane concentration of freshwater channel 'Am Fleet' showing different
326 concentration over time (black dots). Error bars are within the symbols and represent good
327 reproducibility of repeated measurements of minimum 5 samples taken once a day. Dark grey
328 bars and light grey bars indicate daily mean air temperature and precipitation height,
329 respectively.

330 **Discussion**

331 We set up and tested a method using GGA for discrete syringe injections to rapidly and
332 accurately analyze dissolved methane in discrete water samples. It was initially developed to
333 analyze dissolved methane in water samples taken from deep sea hydrocasts using Niskin
334 bottles, available in almost all research vessels. But as shown, the technique can be easily
335 adapted for analyses of water samples from a variety of settings including lakes, aquifers,
336 ponds and estuaries. The reproducibility of the method yield excellent results with values
337 better than 2.5% for different concentrations ranging from 4 to 3200 nM and in samples with

338 salinities ranging from 0 to 35 psu. The precision of the method compares very well with the
339 reported values between 3.3% and 6.8% using headspace equilibration followed by GC
340 injections (Yoshida et al. 2011; Magen et al. 2014; Capelle et al. 2015) and with the precision
341 of 5–10% achieved with the VE-GC method in this study. Reported extraction efficiency for
342 the Vacuum Extraction is 90±6% (Keir et al. 2005, 2009) and, regarding the comparison in
343 Figure 2, the mean outcome from our method is 17 % higher than that for the VE-GC method.

344 The described HS-GGA method using two 140-ml syringes for each sample is appropriate for
345 low methane concentrations, including background seawater values from which methane
346 values in the GGA are an order of magnitude higher than the limit of detection. For higher
347 concentrations, e.g. at gas seepage sites, the range can be easily extended using different
348 volumes of water, headspace and Zero Air. This flexibility allows for methane measurements
349 in most marine and terrestrial settings where dissolved methane concentration is of interest.

350 For the VE-GC all sample bottles have to be evacuated before sampling and vials have to be
351 prepared for sample storage. Both technical steps are relatively time-consuming. Using the
352 headspace method after Magen et al. (2014) samples have to be fixated using chemicals. The
353 shipping and transport of chemicals is always complicated and furthermore, the addition of
354 the NaOH or KOH is another and laborious working step which has to be done after
355 sampling. This work is not necessary for the simple determination of methane concentration.
356 However, if the methane concentration in the samples should be sufficient for conventional
357 isotopic analysis (e.g $\delta^{13}C$-$CH_4$, $\delta^{2}H$-$CH_4$) the Vacuum Extraction method should be
358 considered because methane is not diluted in a headspace. For samples which have to be
359 stored for a longer period the headspace method after Magen et al. (2014) is recommended.

360 The off-axis ICOS technology was originally developed for continuous measurements of air.
361 Since its introduction it has proven useful for continuous analyses of dissolved methane in
362 surface waters using an equilibration set up. With the addition of the method we describe here

to measure discrete samples collected in the water column, the field of application for the GGA is enormous. For example, at seepage sites vertical profiles in the water column can be conducted taking discrete samples. The methane concentration in the surface waters above the seepage system can also be analyzed to generate horizontal transects and these values can be compared with methane concentration in the air above the study site. $CO_2$ concentrations, which are not considered in this study, can also be determined with this instrument. This capability extends the application of the ICOS technology for another important greenhouse gas.

## C**omments and recommendations**

The Greenhouse Gas Analyzer is easy to install and to use, no carrier gas is needed, and allows for field-based analyses of methane over a wide range of concentrations. Field measurements have the advantage of providing immediate results that can guide subsequent sampling and field experimental strategies.

The utilization of syringes with movable piston as sampling devises prevents development of over pressurized headspace. In contrast with the use of vials that require pressure compensation during subsampling, the plunger in the syringe and the valve allow for easy adjustment of the pressures during headspace transfer. We note that small bubbles, which appear in the syringe before shaking, might get lost due to pressure compensation but potential loss of methane was proved to be insignificant by repeated analyses.

Preparation of the sample for injections, including addition of headspace gas, shaking and transferring the gas into the injection syringe, can be done while the instrument analyzes the previous sample (~5 minutes total), so that a mechanical shaker would not necessarily improve efficiency of analyses.

## Acknowledgements

This study was financed by the U.S. Department of Energy Grant #DE-FE00135331. In addition we acknowledge support through DFG Research Center / Cluster of Excellence "The Ocean in the Earth System". We thank the captain and crew members during expeditions M112 and M114 of the R/V Meteor for their outstanding support at sea, and Stephanie Buchheister for her excellent laboratory assistance both at sea and onshore.

## References

Arévalo-Martínez, D. L., M. Beyer, M. Krumbholz, I. Piller, A. Kock, T. Steinhoff, A. Körtzinger, and H. W. Bange. 2013. A new method for continuous measurements of oceanic and atmospheric N 2O, CO and CO2: Performance of off-axis integrated cavity output spectroscopy (OA-ICOS) coupled to non-dispersive infrared detection (NDIR). Ocean Sci. **9**: 1071–1087, doi:10.5194/os-9-1071-2013

Badr, O., S. D. Probert, and P. W. O'Callaghan. 1991. Atmospheric methane: Its contribution to global warming. Appl. Energy **40**: 273–313, doi: 10.1016/0306-2619(91)90021-O

Baer, D. S., J. B. Paul, M. Gupta, and A. O'Keefe. 2002. Sensitive absorption measurements in the near-infrared region using off-axis integrated-cavity-output spectroscopy. Appl. Phys. B Lasers Opt. **75**: 261–265, doi: 10.1007/s00340-002-0971-z

Bange, H. W. 2006. Nitrous oxide and methane in European coastal waters. Estuar. Coast. Shelf Sci. **70**: 361–374, doi: 10.1016/j.ecss.2006.05.042

Bange, H. W., U. H. Bartell, S. Rapsomanikis, and M. O. Andreae. 1994. Methane in the Baltic and North Seas and a reassessment of the marine emissions of methane. Global Biogeochem. Cycles **8**: 465–480, doi: 10.1029/94GB02181

409 Berman, E. S. F., M. Fladeland, J. Liem, R. Kolyer, and M. Gupta. 2012. Greenhouse gas
410 analyzer for measurements of carbon dioxide, methane, and water vapor aboard an
411 unmanned aerial vehicle. Sensors Actuators, B Chem. **169**: 128–135, doi:
412 10.1016/j.snb.2012.04.036

413 Biastoch, A., T. Treude, L. H. Rüpke, U. Riebesell, C. Roth, E. B. Burwicz, W. Park, M.
414 Latif, C. W. Böning, G. Madec, and K. Wallmann. 2011. Rising Arctic Ocean
415 temperatures cause gas hydrate destabilization and ocean acidification. Geophys. Res.
416 Lett. **38**, doi:10.1029/2011GL047222

417 Bohrmann, G., Alvarez, R., Biller, T., Buchheister, S., Büttner, H., Canoni, O., Dehning, K.,
418 T. Ferreira, C., Geprägs, P., Heinken, S., Hüttich, D., Johansen, C., Klar, S., Klüber, S.,
419 Leymann, D. Mai, H.A., Marcon, Y., Mary, F., Meinecke, G., Menapace, W., Nowald,
420 N., Pape, T., Praeg, H. Raeke, A., Rehage, R., Renken, J., Reuter, C., Rohleder, C.,
421 Römer, M., Sahling, M. Sans i Coll, C., Schade, T., Seiter, C., Spalek, P., Spiesecke, U.,
422 Tamborrino, L., Torres, M.E., von Wahl, T., Wiebe, M., Wintersteller, P., Zarrouk. 2014.
423 Report and preliminary results of R/V METEOR cruise M112, Dynamic of Mud
424 Volcanoes and Seeps in the Calabrian Accretionary Prism, Ionian Sea, Catania (Italy) –
425 Catania (Italy), November 6 – December 15.

426 Capelle, D. W., J. W. Dacey, and P. D. Tortell. 2015. An automated, high through-put method
427 for accurate and precise measurements of dissolved nitrous-oxide and methane
428 concentrations in natural waters. Limnol. Oceanogr. Methods n/a–n/a, doi:
429 10.1002/lom3.10029

430 Clark, J. F., I. Leifer, L. Washburn, and B. P. Luyendyk. 2003. Compositional changes in
431 natural gas bubble plumes: Observations from the coal oil Point marine hydrocarbon
432 seep field. Geo-Marine Lett. **23**: 187–193, doi: 10.1007/s00367-003-0137-y

433 Currie, L. A. 1968. Limits for qualitative detection and quantitative determination.
434 Application to radiochemistry. Anal. Chem. **40**: 586–593, doi: 10.1021/ac60259a007

435 Damm, E., E. Helmke, S. Thoms, U. Schauer, E. Nöthig, K. Bakker, and R. P. Kiene. 2009.
436 Methane production in aerobic oligotrophic surface water in the central Arctic Ocean.
437 Biogeosciences Discuss. **6**: 10355–10379, doi: 10.5194/bgd-6-10355-2009

438 Greinert, J., and D. F. McGinnis. 2009. Single bubble dissolution model - The graphical user
439 interface SiBu-GUI. Environ. Model. Softw. **24**: 1012–1013, doi:
440 10.1016/j.envsoft.2008.12.011

441 Gülzow, W., G. Rehder, B. Schneider, J. S. V. Deimling, and B. Sadkowiak. 2011. A new
442 method for continuous measurement of methane and carbon dioxide in surface waters
443 using off-axis integrated cavity output spectroscopy (ICOS): An example from the Baltic
444 Sea. Limnol. Oceanogr. Methods **9**: 176–184, doi: 10.4319/lom.2011.9.176

445 Holmes, M. E., F. J. Sansone, T. M. Rust, and B. N. Popp. 2000. Methane production ,
446 consumption , and air-sea exchange in the open ocean : An evaluation based on carbon
447 isotopic ratios and Brian via the upper mixed layer at a rate value of ap-. Global
448 Biogeochem. Cycles **14**: 1–10, doi: 10.1029/1999GB001209

449 IPCC. 2007. Climate Change 2007: The Physical Science Basis. Contribution of Working
450 Group I to the Fourth Assessment Report of the Intergovernmental Panel on Climate
451 Change, K.B.A. Solomon, S., D. Qin, M. Manning, Z. Chen, M. Marquis and M.T. and
452 H.L. Miller [eds.]. Cambridge University Press.

453 IPCC. 2013. Climate Change 2013: The Physical Science Basis. Contribution of Working
454 Group I to the Fifth Assessment Report of the Intergovernmental Panel on Climate

455 Change, V.B. and P.M.M. Stocker, T.F., D. Qin, G.-K. Plattner, M. Tignor, S.K. Allen,
456 J. Boschung, A. Nauels, Y. Xia [eds.]. Cambridge University Press.

457 Keir, R. S., J. Greinert, M. Rhein, G. Petrick, J. Sültenfuß, and K. Fürhaupter. 2005. Methane
458 and methane carbon isotope ratios in the Northeast Atlantic including the Mid-Atlantic
459 Ridge (50°N). Deep. Res. Part I Oceanogr. Res. Pap. **52**: 1043–1070.

460 Keir, R. S., O. Schmale, R. Seifert, and J. Sültenfuß. 2009. Isotope fractionation and mixing
461 in methane plumes from the Logatchev hydrothermal field. Geochemistry, Geophys.
462 Geosystems **10**, doi:10.1029/2009GC002403

463 Lammers, S., and E. Suess. 1994. An improved head-space analysis method for methane in
464 seawater. Mar. Chem. **47**: 115–125, doi: 10.1016/0304-4203(94)90103-1

465 Li, Y., L. Zhan, J. Zhang, and L. Chen. 2015. Equilibrator-based measurements of dissolved
466 methane in the surface ocean using an integrated cavity output laser absorption
467 spectrometer. Acta Oceanol. Sin. **34**: 34–41, doi: 10.1007/s13131-015-0685-9

468 Magen, C., L. L. Lapham, J. W. Pohlman, K. Marshall, S. Bosman, M. Casso, and J. P.
469 Chanton. 2014. A simple headspace equilibration method for measuring dissolved
470 methane. Limnol. Oceanogr. Methods **12**: 637–650, doi: 10.4319/lom.2014.12.637

471 Mau, S., D. L. Valentine, J. F. Clark, J. Reed, R. Camilli, and L. Washburn. 2007. Dissolved
472 methane distributions and air-sea flux in the plume of a massive seep field, Coal Oil
473 Point, California. Geophys. Res. Lett. **34**: 2–6, doi:10.1029/2007GL031344

474 McGinnis, D. F., J. Greinert, Y. Artemov, S. E. Beaubien, and A. Wüest. 2006. Fate of rising
475 methane bubbles in stratified waters: How much methane reaches the atmosphere? J.
476 Geophys. Res. Ocean. **111**: 1–15, doi: 10.1029/2005JC003183

Pape, T., A. Bahr, J. Rethemeyer, J. D. Kessler, H. Sahling, K. U. Hinrichs, S. A. Klapp, W. S. Reeburgh, and G. Bohrmann. 2010. Molecular and isotopic partitioning of low-molecular-weight hydrocarbons during migration and gas hydrate precipitation in deposits of a high-flux seepage site. Chem. Geol. **269**: 350–363, doi: 10.1016/j.chemgeo.2009.10.009

Reeburgh, W. 2007. Oceanic methane biogeochemistry. Chem. Rev. 486–513, doi: 10.1021/cr050362v

Rehder, G., R. S. Keir, E. Suess, and M. Rhein. 1999. Methane in the northern Atlantic controlled by microbial oxidation and atmospheric history. Geophys. Res. Lett. **26**: 587, doi: 10.1029/1999GL900049

Rella, C. W., H. Chen, A. E. Andrews, A. Filges, C. Gerbig, J. Hatakka, A. Karion, N. L. Miles, S. J. Richardson, M. Steinbacher, C. Sweeney, B. Wastine, and C. Zellweger. 2013. High accuracy measurements of dry mole fractions of carbon dioxide and methane in humid air. Atmos. Meas. Tech. **6**: 837–860, doi: 10.5194/amt-6-837-2013

Schmale, O., J. Schneider von Deimling, W. Gülzow, G. Nausch, J. J. Waniek, and G. Rehder. 2010. Distribution of methane in the water column of the Baltic Sea. Geophys. Res. Lett. **37**, doi: 10.1029/2010GL043115

Traganza, E. D., J. W. Swinnerton, and C. H. Cheek. 1979. Methane supersaturation and ATP-zooplankton blooms in near-surface waters of the Western Mediterranean and the subtropical North Atlantic Ocean. Deep Sea Res. Part A. Oceanogr. Res. Pap. **26**: 1237–1245, doi: 10.1016/0198-0149(79)90066-9

Tsurushima, N., S. Watanabe, and S. Tsunogai. 1996. Methane in the East China Sea water. J. Oceanogr. **52**: 221–233, doi: 10.1007/BF02235671

500 Valentine, D. L. 2011. Emerging topics in marine methane biogeochemistry. Ann. Rev. Mar.
501 Sci. **3**: 147–171, doi: 10.1146/annurev-marine-120709-142734

502 Welp, L. R., R. F. Keeling, R. F. Weiss, W. Paplawsky, and S. Heckman. 2013. Design and
503 performance of a Nafion dryer for continuous operation at CO2and CH4 air monitoring
504 sites. Atmos. Meas. Tech. **6**: 1217–1226, doi: 10.5194/amt-6-1217-2013

505 Yamamoto, S., J. B. Alcauskas, and T. E. Crozier. 1976. Solubility of methane in distilled
506 water and sea water. J. Chem. Eng. Data **21**: 78–80, doi: 10.1021/je60068a029

507 Yoshida, O., H. Y. Inoue, S. Watanabe, K. Suzuki, and S. Noriki. 2011. Dissolved methane
508 distribution in the South Pacific and the Southern Ocean in austral summer. J. Geophys.
509 Res. Ocean. **116**: 1–9, doi: 10.1029/2009JC006089

510

511

Transport in Porous Media

# Methane hydrate formation under conditions of variable salinity II. Time-stepping variants and sensitivity of reduced numerical model

--Manuscript Draft--

| | |
|---|---|
| **Manuscript Number:** | |
| **Full Title:** | Methane hydrate formation under conditions of variable salinity II. Time-stepping variants and sensitivity of reduced numerical model |
| **Article Type:** | Original Research Paper |
| **Keywords:** | methane hydrate formation; numerical discretization; implicit and non-implicit time-stepping; model sensitivity and convergence; multiphase multicomponent model |
| **Corresponding Author:** | Malgorzata Peszynska, PhD, Dr. hab<br>Oregon State University<br>Corvallis, OR UNITED STATES |
| **Corresponding Author Secondary Information:** | |
| **Corresponding Author's Institution:** | Oregon State University |
| **Corresponding Author's Secondary Institution:** | |
| **First Author:** | Malgorzata Peszynska, PhD, Dr. hab |
| **First Author Secondary Information:** | |
| **Order of Authors:** | Malgorzata Peszynska, PhD, Dr. hab<br>Francis Patricia Medina, PhD<br>Wei-Li Hong, PhD<br>Marta E. Torres, PhD |
| **Order of Authors Secondary Information:** | |
| **Funding Information:** | National Science Foundation (US) (DMS-1115827, DMS-1522734) — Professor Malgorzata Peszynska<br>U.S. Department of Energy (US) (DE-FE00135331) — Marta E. Torres<br>Research Council of Norway (223259) — Wei-Li Hong |
| **Abstract:** | In this paper we consider a reduced model of methane hydrate formation in variable salinity conditions presented in a companion paper, and give details on discretization and three time-stepping variants: Implicit, Semi-implicit, and Sequential. We compare their accuracy and efficiency depending on the spatial and temporal discretization parameters. We also study sensitivity of the model to the simulation parameters and in particular to the reduced phase equilibria model. |
| **Suggested Reviewers:** | Rainer Helmig, PhD<br>Professor, Universitat Stuttgart<br><br>Expert in numerical modeling of flow and transport in porous media |
| | Stephen Bryant<br>The University of Texas at Austin<br><br>Leader in reservoir simulation with knowledge of hydrates |
| | Inse Neuweiler<br>Professor, Universitat Stuttgart<br><br>Dynamic researcher on numerical modeling of multiphase multicomponent models |

Powered by Editorial Manager® and ProduXion Manager® from Aries Systems Corporation

| | |
|---|---|
| | Eleanor Jenkins, PhD<br>Professor, Clemson University<br><br>Expert on time stepping and nonlinear solvers for complex flow problems |

*Powered by Editorial Manager® and ProduXion Manager® from Aries Systems Corporation*

Manuscript
Click here to download Manuscript: PHMT.pdf
Click here to view linked References

**Noname manuscript No.**
(will be inserted by the editor)

# Methane hydrate formation under conditions of variable salinity II. Time-stepping variants and sensitivity of reduced numerical model

**Malgorzata Peszynska · Francis Patricia Medina · Wei-Li Hong · Marta E. Torres**

the date of receipt and acceptance should be inserted later

Received: date / Accepted: date

**Abstract** In this paper we consider a reduced model of methane hydrate formation in variable salinity conditions presented in a companion paper, and give details on discretization and three time-stepping variants: Implicit, Semi-implicit, and Sequential. We compare their accuracy and efficiency depending on the spatial and temporal discretization parameters. We also study sensitivity of the model to the simulation parameters and in particular to the reduced phase equilibria model.

**Keywords** methane hydrate · flow and transport · subsea porous sediment · phase equilibria · salinity

**Mathematics Subject Classification (2000)** MSC 65M06 · 76S05 · MSC 76V05 · 35R35

M. Peszynska and F.P. Medina's research was partially supported by the NSF DMS-1115827 "Hybrid modeling in porous media" and DMS-1522734 "Phase transitions in porous media across multiple scales". M. Torres and W.-L. Hong were supported by US Department of Energy grant #DE-FE00135331 and by the Research Council of Norway through its Centres of Excellence funding scheme, project 223259.

M. Peszynska
Department of Mathematics, Oregon State University, USA. E-mail: mpesz@math.oregonstate.edu

F. P. Medina
Department of Mathematics, Oregon State University, USA. E-mail: medinaf@math.oregonstate.edu

W.-L. Hong
College of Earth, Ocean, and Atmospheric Sciences, Oregon State University, USA.
CAGE (Centre for Arctic Gas Hydrate, Environment and Climate), Department of Geology, UiT The Arctic University of Norway, Tromso, Norway E-mail: wei.l.hung@uit.no

M. Torres
College of Earth, Ocean, and Atmospheric Sciences, Oregon State University, USA. E-mail: mtorres@coas.oregonstate.edu

## 1 Introduction

In the paper [18] we introduced a reduced model for methane hydrate formation in variable salinity conditions and provided details on the equilibrium phase behavior adapted to a case study from Ulleung Basin. One of the advantages of this reduced model in contrast to fully comprehensive models is that the reduced model is easy to implement and to extend, and is amenable to various analyses.

In this paper we describe the computational aspects of the model, with emphasis placed on the variants of time-stepping. Our reduced model accounts for three components: water, methane, and salt, and two phases: aqueous, and solid (hydrate). Thus, it places in the general framework of multiphase multicomponent models such as those in [12,10,3] for which accuracy and efficiency have been studied extensively in the past decades. In particular, for the oil-water or black-oil models described e.g. in [27,2,15,20,31,30] the best practice is to use mass-conservative spatial schemes combined either with an implicit treatment of pressures and explicit treatment of saturations/concentrations, or with a fully implicit treatment of all phases and components. Typically, the computational complexity of implicit models is the highest, while other variants are easier to implement. In compositional models [4] with $M$ components the pressure solver is complemented with $M$-1 transport equations solved for concentration of the selected $M$-1 species, and followed by flash, i.e., the equilibrium solver. The typical time scales of interest for reservoir simulation with these models are days to decades of production or environmental remediation. On the other hand, in [18] and here we are interested in long time behavior and hydrate basin modeling, and it makes sense to assume that the pressures and temperatures are known and given by hydrostatic and geothermal distributions. Our models need only to resolve the interdependence between methane and water phase equilibria that depend on the presence of salt, and our time-stepping algorithms have different features than those for the oil-gas reservoir simulators.

We implement the interdependence between the components and phases as follows. The water-methane-salt equilibria are handled using the approach of nonlinear complementarity constraints, and are either tightly or loosely coupled to the salt mass conservation; their implementation is especially easy with the reduced phase behavior model adopted in [18]. We consider and compare three variants of time-stepping that realize these tight or loose couplings: the fully implicit (I), semi-implicit (SI), and sequential (SEQ) algorithms. The comparison that we carry out is intended to demonstrate the merits of these approaches, and guide the choice of a model.

In addition, in this paper we test the sensitivity of the approach to the assumed phase behavior model, as well as to various parameters defining the discretization. The latter is new and was not undertaken for the comprehensive model [14]. It is significant in that it guides the reader in the choice of optimal parameters and shows the robustness of the reduced model.

| Symbol | Definition | Units/ value |
|---|---|---|
| | **Data about reservoir and fluids** | |
| $x = (x_1, x_2, x_3)$ | Spatial coordinate | [m] |
| $t$ | Time variable | [yr] |
| $G$ | Gravitational acceleration | 9.8 m/s$^2$ |
| $D(x)$ | Depth of point $x$ from sea level | [m] |
| $D_{ref}(x)$ | Seafloor depth | [m] |
| | In 1D case $x = x_3$, $H = D_{ref}$ | |
| $z = D(x_3) - H$ | Depth below seafloor | [m] |
| (G)HSZ | (Gas) Hydrate stability zone | |
| $P$ | Pressure | [Pa,MPa] |
| $G_H$ | Hydrostatic gradient | $\approx 10^4$Pa/m |
| $T$ | Temperature | [K] |
| $G_T$ | Geothermal gradient | [K/m] |
| $q$ | Darcy volumetric flux of liquid phase | [m/yr] |
| $D_M = D_S = D^0 S_l \phi_0$ | Diffusivity of component $C$ in the liquid phase | [m$^2$/yr] |
| | $D^0 = 10^{-9}$m$^2$/s $= 3 \times 10^{-2}$m$^2$/yr | |
| $\rho_l$ | Seawater density | 1030 kg/m$^3$ |
| $\rho_h$ | Hydrate density | 925 kg/m$^3$ |
| $\chi_{hM}$ | Mass fraction of methane in hydrate phase | 0.134 kg/kg |
| $R = \chi_{hM}\rho_h/\rho_l$ | Constant used for methane concentration | 0.1203 kg/kg |
| $\phi_0, \phi = S_l\phi_0$ | Porosity in $\Omega$ without/with hydrate present | |
| $K_0, K$ | Permeability in $\Omega$ without/with hydrate present | |
| $\chi_{lS}^{sw}$ | Seawater salinity | $0.035[kg/kg]$ |
| $f_M$ | Supply of methane (source/sink term) | [kg/kg/yr] |
| $\alpha$ | Parameter of the reduced model | [kg/kg] |
| | **Variables in the model** | |
| $S_l, S_h = 1 - S_l$ | Void fraction of liquid and hydrate phases | |
| $\chi_{lM}$ | Mass fraction of methane (solubility) in liquid phase | [kg/kg] |
| $\chi_{lS}$ | Mass fraction of salt (salinity) in liquid phase | [kg/kg] |
| $N_M, N_S$ | Mass concentration of methane and salt | [kg/kg] |
| | per kg of liquid phase | |

**Table 1** Notation and definitions

The paper is organized as follows. In Sec. 2 we briefly recall the model proposed in [18] including the phase behavior. In Sec. 3 we describe in detail the time-stepping variants and spatial discretization for that model. In Sec. 4 we compare the I, SI, and SEQ time-stepping variants, and in Sec. 5 we discuss the sensitivity of the model to the various parameters of the computational model. We conclude in Sec. 6.

## 2 Mathematical model

In the last decade two classes of models for hydrates have been used to describe hydrate behavior in natural systems. These are the fully comprehensive equilibrium models such as [14], and the simpler conceptual models [32, 16, 26], in which simplified mechanisms for fluid equilibria and/or kinetics were assumed. The model presented in [18] and discussed here falls somewhere inbetween, and is a direct simplification of the comprehensive model in [14]. The simplicity of the reduced model allows for rigorous mathematical well-posedness analysis in

the case of the diffusive transport in [9], and more general analysis in [21] for advective/diffusive transport.

We start with Tab. 1, which summarizes the definitions and the notation consistent with that used in [18].

We consider the transport of methane and salt in the sediment reservoir $\Omega \subset \mathbb{R}^d, d = 1, 2, 3$. Each point $x = (x_1, x_2, x_3) \in \Omega$ is at some depth $D(x)$ below the sea surface, with the origin $x = 0$ beneath the reservoir but above the bottom of the GHSZ, with a fixed reference depth $D_{ref} = H$ equal to the water depth $H$ at seafloor, i.e., at the top of the reservoir $\Omega$.

In this paper as in [18] we assume that the conditions in $\Omega$ are favorable for hydrate presence and that $\Omega$ is entirely within the GHSZ, while the methane is suplied by advection and diffusion from beneath GHSZ. The actual porosity $\phi(x)$ available to the liquid phase at $x$ is $\phi = \phi_0 S_l$, where $S_l$ is the liquid phase saturation, i.e., void fraction of the liquid phase. The actual permeability $K(x)$ in the presence of hydrate is an important property but is not needed in the 1D model with constant flux.

First, we assume that $T(x)$ is known and follows the geothermal gradient

$$T(x) = T_{ref} + (D(x) - D_{ref})G_T, \tag{1}$$

where $T_{ref}$ is the temperature at some reference depth $D_{ref}$ and $G_T \approx const$ is the geothermal gradient; see [18] for experimental values. The pressure $P(x)$ is assumed close to the hydrostatic

$$P(x) \approx P_l^0(x) := P_l^0|_{D_{ref}} + \rho_l G(D(x) - D_{ref}). \tag{2}$$

Here $P_l^0$ is known at the reference depth $D_{ref}$.

### 2.1 Mass conservation

In region $\Omega$ we have the following mass conservation equations for methane and salt components, respectively

$$\frac{\partial \phi_0 N_M}{\partial t} - \nabla \cdot D_M \nabla \chi_{lM} + \nabla \cdot (q \chi_{lM}) = f_M, \tag{3a}$$

$$\frac{\partial \phi_0 N_S}{\partial t} - \nabla \cdot D_S \nabla \chi_{lS} + \nabla \cdot (q \chi_{lS}) = 0, \tag{3b}$$

with the definitions

$$N_M = S_l \chi_M + R(1 - S_l), \tag{3c}$$

$$N_S = \chi_{lS} S_l. \tag{3d}$$

where $R$ is given in Tab. 1. The model is complemented by a pressure equation or $q$ must be given; here we assume the latter. As we explain in [18], the model (3) arises as a special case of the first-principles comprehensive model in [14].

We see that in (3) we have two mass conservation equations (3a)-(3b) with three unknowns that must be chosen from $N_M, N_S, \chi_{lS}, \chi_{lM}$ and $S_l$. To close the system we use the [NCC-M] phase constraint.

## 2.2 Phase equilibria and [NCC-M] constraint

The (maximum) amount $\chi_{lM}^{max}$ of methane that can be dissolved in the liquid phase depends on the pressure $P$, temperature $T$, and the salinity $\chi_{lS}$. Equivalently, these variables determine the circumstances in which $S_l < 1$ and $S_h > 0$, i.e., when the hydrate phase can be present. In addition, $\chi_{lM}^{max}$ determines how the total amount of methane $N_M$ is partitioned between the liquid and hydrate phases. This phase equilibrium is expressed concisely as a nonlinear complementarity constraint [NCC-M]

$$\begin{cases} \chi_{lM} \le \chi_{lM}^{max}, & S_l = 1\,, \\ \chi_{lM} = \chi_{lM}^{max}, & S_l \le 1\,, \\ (\chi_{lM}^{max} - \chi_{lM})(1 - S_l) & = 0\,. \end{cases} \tag{3e}$$

In other words, if $N_M(x,t)$ is small enough so that $N_M < \chi_{lM}^{max}$, then only the liquid phase is present $S_l(x,t) = 1$, and $\chi_{lM} = N_M$ is the independent variable that describes how much methane is dissolved in the liquid. On the other hand, when the amount present $N_M \ge \chi_{lM}^{max}$, the excess amount of methane above $\chi_{lM}^{max}$ forms the hydrate phase with $S_h = 1 - S_l > 0$, and $S_l < 1$ becomes the independent variable while $\chi_{lM} = \chi_{lM}^{max}$. This relationship has to be satisfied at every point $x, t$.

### *2.2.1 Data for $\chi_{lM}^{max}$*

In the hydrate literature [14, 25] there are tabulated data, or algebraic models, for how $\chi_{lM}^{max}$ depends on $P, T, \chi_{lS}$. In addition, there may be dependence of (3e) on the type of sediment [5, 23] but this is out of scope here. In [18] we developed a particular approximation

$$\chi_{lM}^{max} \approx \chi_{lM}^{max}(x, \chi_{lS}) \approx \chi_{lM}^{max,0}(x) + \alpha(x)\chi_{lS}, \tag{4}$$

in which the data $\chi_{lM}^{max,0}(x)$ and $\alpha(x)$ must be provided. This approximation (4) includes as a special case the algebraic model in [23]. In [18] we describe how to obtain $\chi_{lM}^{max,0}(x)$ and $\alpha(x)$ by a fit to the lookup tables extracted from the well known phase equilibrium software CSMGem [1], and we calibrate them for the typical depth, temperature, and salinity conditions found in Ulleung Basin; see the plot of $\chi_{lM}^{max,0}(x)$ and $\alpha(x)$ in Fig. 6. As is well known, $\chi_{lM}^{max,0}$ increases with depth, thus decreases with $x$. On the other hand, $\alpha(x)$ found with CSMGem is positive while the authors in [33] believe it should be negative; see [18] for details. In Sec. 5 we discuss the sensitivity of the model to the assumed profile of $\alpha(x)$.

### *2.2.2 Other constraints*

There are additional constraints that are not part of the model (3). In particular, we must have $S_h \le 1$ or

$$S_l \ge 0, \chi_{lM} \ge 0. \tag{5}$$

With some assumptions on $\chi_{lM}^{max}$, the boundary and initial data, and small $f_M, q$ one can prove that (5) holds as a consequence of the maximum principle and other abstract analyses. (See [9] for the diffusive case and [21] for advective and diffusive transport case). In other circumstances (5) may not necessarily hold, and a numerical model may produce $S_h$ increasing to 1 and beyond. This clearly is nonphysical, since even before the pores become plugged up and $\phi = S_l\phi_0 = 0$, all the flow and diffusion ceases, local pressures increase, and the sediment may break. When (5) is violated, a more general model than (3), e.g., including geomechanics and pore-scale effects, should be considered; see, e.g., the mathematical model in [5]. In this paper we terminate the simulation when $S_h$ is close to 1.

### 2.3 Boundary and initial conditions

The model (3) must be supplemented with appropriate initial conditions imposed on $N_M$ and $N_S$, and the boundary conditions on the fluxes or on the values of the transport variables $\chi_{lM}$ and $\chi_{lS}$. In this paper we set

$$N_M(x,0) = N_M^0(x), \quad N_S(x,0) = N_S^0(x), \quad x \in \Omega \tag{6a}$$

$$\chi_{lM}(0,t) = \chi_{lM}^0, \quad \chi_{lM}(L,t) = \chi_{lM}^L = 0, \quad t > 0 \tag{6b}$$

$$\chi_{lS}(0,t) = \chi_{lS}^0, \quad \chi_{lS}(L,t) = \chi_{lS}^L \chi_{lS}^{sw}, \quad t > 0 \tag{6c}$$

The conditions (6c) assign the seawater salinity at $x = L$ and some other salinity $\chi_{lS}^0$ at HSZ known from observations. The conditions (6b) assume some methane present at HSZ $x = 0$, and that there is no methane in the ocean at $x = L$. The choice consistent with (4)

$$\chi_{lM}^0 = \chi_{lM}^{max,0}(0) + \alpha(0)\chi_{lS}^0 \tag{7}$$

allows the maximum possible amount of methane to be transported by advection and diffusion from underneath the HSZ.

## 3 Numerical model

Now we provide details of the numerical model for (3). We use mass-conservative spatial discretization based on cell-centered finite differences (FD) with harmonic averaging and a nonuniform structured spatial grid. An alternative discretization of the case $q = 0$, with Finite Elements and mass lumping, was considered in [9], but it would not accomodate large advective fluxes and is not locally mass conservative. For time discretization we use operator splitting: we treat advection explicitly and diffusion implicitly as in [6,7,29]. The diffusion/equilibria handle two components and are organized in several time-stepping variants. In each variant we have to solve a linear or nonlinear system of equations; for the latter we use Newton (or semismooth Newton) iteration.

### 3.1 Implementing phase constraint [NCC-M]

While it is well known how to discretize and solve advection-diffusion equations, implementing phase equilibria constraint (3e) is challenging, but there are several approaches known from constrained optimization [11,28].

First, the constraint (3e) can be rewritten using the notion of active/inactive sets [11]. In this approach at each time step and/or iteration, the (grid) points are identified as either those for which the first part of the inequality (3e) holds, or those where the other complementary inequality must hold. Next the mass conservation equations are specialized depending on the state of the primary unknowns, and are grouped together and solved for the particular active set of independent unknowns. The equivalent approach is that of variable switching [3,14] where at each gridpoint one identifies the appropriate independent variable depending on which of the inequalities holds.

Yet another equivalent approach which we find the easiest to implement [9] takes advantage of the semismooth "min" function as proposed in [8]. We use

$$\min(\chi_{lM}^{max} - \chi_{lM}, 1 - S_l) = 0, \tag{8}$$

which is equivalent to (3e). We recall that the function "min(u,v)" equals $u$ if $u \leq v$ and $v$ otherwise; it is therefore piecewise linear and non-differentiable along $u = v$, hence the name semismooth.

Equation (8) is a nonlinear equation in the variables $\chi_{lM}$ and $S_l$, and it provides the fifth equation to complement (3a)-(3d) that can be solved together for the five unknowns $N_M, N_S, \chi_{lM}, \chi_{lS}, S_l$. Some of the time-stepping variants require also local nonlinear solvers called "flash" which are invoked at a particular grid point.

*Simple flash.* The simplest situation is when $N_M$ is known and we know $\chi_{lM}^{max}$. To determine $S_l$ and $\chi_{lM}$ we simply use (3e) and (3c) to calculate

$$S_l = \frac{N_M - R}{\chi_{lM} - R} = \begin{cases} 1, & N_M \leq \chi_{lM}^{max}(x,t), \\ \frac{N_M - R}{\chi_{lM}^{max}(x,t) - R}, & N_M > \chi_{lM}^{max}(x). \end{cases} \tag{9}$$

Simple flash only is applicable if salinity is fixed because of the dependence of $\chi_{lM}$ on $\chi_{lS}$.

*Two-variable flash.* Given $N_M, N_S$ we can solve for the three unknowns $S_l$, $\chi_{lM}$, $\chi_{lS}$ using (3c), (3d) and (8). The implementation is especially easy if (4) is used. This flash solver typically takes 2 or 3 iterations to complete, but may fail when $S_h$ is close to 1.

### 3.2 Notation in fully discrete model

The notation for discretization is straightforward. We find approximations to the relevant variables at discrete time steps $t_1, t_2, \dots t_n, \dots$. The transport model (3) advances the model variables from $t_n$ to $t_{n+1}$, with the time step $\tau = t_{n+1} - t_n$ considered uniform for simplicity. Also for simplicity, we consider the 1D reservoir $\Omega = \bigcup_i \Omega_i$, where $\Omega_i$ are the cells with the centers $x_i$ and uniform length $h$, and $i = 1, \dots N_x$. We approximate $N_M(x_i, t_n) \approx N^n_{M,i}$ and set $N^n_M$ to be a vector of $N^n_{M,i}$, with analogous notation applied to other variables.

We start by integrating each of the mass conservation equations over each $\Omega_i$. We show the calculations for methane; the ones for salt are analogous.

*Accumulation and source terms.* For each $i, n$ we calculate the approximation of accumulation and source terms as follows

$$\int_{\Omega_i} \phi_0 N_M(x, t^n) dx \approx \phi_0(x_i) N^n_{M,i} h. \quad \int_{\Omega_i} f_M(x) dx \approx h f_{M,i}. \tag{10}$$

*Advection terms.* It suffices to consider only methane advection. We consider first the case $q > 0$. The advective flux

$$\int_{\Omega_i} \nabla \cdot (q \chi_{lM}(x, t^n)) dx \approx q(\chi^n_{lM,i} - \chi^n_{lM,i-1}) \tag{11}$$

is handled by upwinding. Close to the inflow boundary at $i = 1$, we set $\chi^n_{lM,0}$ to the boundary value $\chi^0_{lM}$. If $q < 0$, we replace the right hand side by $\chi^n_{lM,i+1} - q\chi^n_{lM,i}$, and use the boundary condition $\chi^L_{lM}$ on top of the reservoir.

*Diffusion terms.* For the spatially dependent diffusion coefficient $D_M(x)$ and the variable $\chi_{lM}(x)$ we have, in a standard way [17,24]

$$\begin{aligned} &- \int_{\Omega_i} \nabla \cdot D_M \nabla \chi_{lM} dx \\ &\quad \approx -h \left( \frac{D_{M,i+1/2}(\chi_{lM,i+1} - \chi_{lM,i}) - D_{M,i-1/2}(\chi_{lM,i} - \chi_{lM,i-1})}{h^2} \right) \end{aligned} \tag{12}$$

where $D_{M,i+1/2}, D_{M,i-1/2}$ are found by harmonic averaging of the values $D_{M,i}, D_{M,i+1}$ and $D_{M,i}, D_{M,i-1}$, respectively. Close to the boundary we apply the discretization described in [19], e.g., at $i = 1$ in place of $\chi_{lM,0}$ we use the boundary value $\chi^0_{lM}$, with $D_{M,1/2}$ set to $2D_{M,1}$.

We also define the discrete diffusion matrix $A$ with the entries defined so that $h(A\chi_{lM})_i$ is equal to the right hand side of (12). In particular, $A_{ii} = \frac{D_{M,i-1/2} + D_{M,i+1/2}}{h^2}$. With Dirichlet boundary conditions $A$ is symmetric and positive definite, as long as $D > 0$. In 1d $A$ is also tridiagonal. Further, since $D_M$ depends on $\phi_0 S_l$ as in Tab. 1, the matrix $A = A(S_l)$ depends on the local saturation values. Finally, since $D_M = D_S$ and the type of boundary conditions on $\chi_{lM}$ matches that for $\chi_{lS}$, the matrix for salt equation is the same as that for methane.

### 3.3 Advection step

The time-stepping variants considered in this paper are explicit in the advection. This allows development of higher-order schemes as well as avoids additional numerical diffusion associated with implicit treatment of advection [6,7,29]. With this step, we have to consider appropriate boundary conditions which in the operator splitting come from (6b)–(6c); in the advection step we can only impose the boundary condition on the inflow boundary.

In the 1D case considered here $\nabla \cdot q = 0$ implies that $q$ is constant, thus the inflow boundary is determined by the sign of $q$. If $q > 0$, the inflow bundary is at the bottom of the reservoir at $x = 0$, otherwise it is at $x = L$. In the advection step, we must know $\chi_{lM}$ and $\chi_{lS}$ on the inflow boundary, and we use here exactly two of (6b)–(6c).

The advection step is as follows. Given $N_M^n$ from previous time step, with the corresponding $\chi_{lM}^n$, we can easily calculate $N_M^{n+1/2}$

$$\frac{\phi_0 N_M^{n+1/2} - \phi_0 N_M^n}{\tau} + \nabla \cdot (q \chi_{lM}^n) = 0 \tag{13a}$$

where the terms $\nabla\cdot$ are approximated by (11). Rearranging (13a) we obtain an explicit expression for the methane amount $\phi_0 N_{M,i}^{n+1/2}$ at the intermediate auxiliary time $t^{n+1/2}$

$$\phi_0 N_{M,i}^{n+1/2} = \phi_0 N_{M,i}^n - \frac{q\tau}{h_i}(\chi_{M,i}^n - \chi_{M,i-1}^n) = 0. \tag{14}$$

As is well known, stability of this explicit advection scheme requires that

$$\frac{|q|\tau}{\phi h} \leq 1 \tag{15}$$

via the well-known Courant-Friedrichs-Lévy (CFL) condition [13] adapted to porous media.

Advection scheme for $N_S^{n+1/2}$ is defined analogously to (14).

### 3.4 Diffusion step

Knowing $N_M^{n+1/2}$ and $N_S^{n+1/2}$ from the advection step, we solve the coupled diffusion/phase behavior system for $N_M^{n+1}$ and $N_S^{n+1}$ with the boundary conditions (6b)–(6c). To distinguish between the variants and avoid additional superscripts, we reserve the notation $N_M^{n+1}$ and $N_S^{n+1}$ for the solutions to the fully implicit variant I.

First we recall that with (12) and matrix $A$ we have the vector equation

$$\frac{\phi_0 N_M^{n+1} - \phi_0 N_M^{n+1/2}}{\tau} + A(S_l^n)\chi_{lM}^{n+1} = f_M^{n+1}. \tag{16}$$

Note the time lagging of the dependence of matrix $A$ on $S_l$.

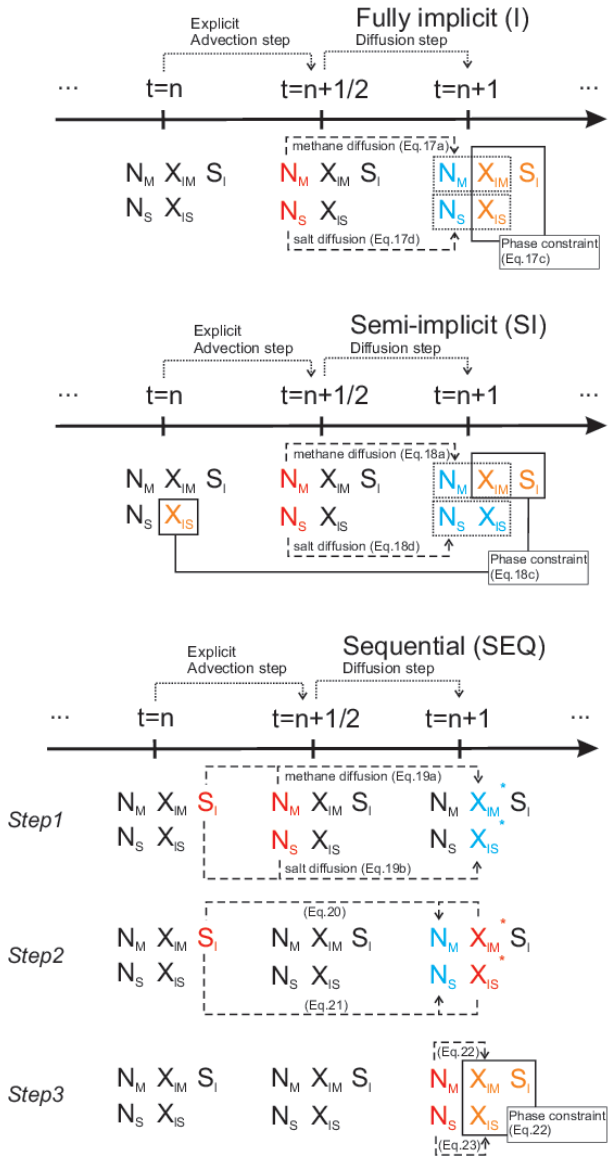


**Fig. 1** Illustration of time stepping variants.

For $N_S^{n+1}$ we have an equation analogous to (16). Additionally, we need to account for [NCC-M]. This coupled system of two component diffusion and phase equilibria is solved with one of the three variants: fully implicit (I), semi-implicit (SI), and sequential (SEQ). See Fig. 1 for graphical illustration of the operator splitting and different variants.

### *3.4.1 Variant (I): fully implicit*

The fully implicit variant solves the coupled two-component diffusion/phase behavior system for $(S_l^{n+1}, \chi_{lM}^{n+1}, \chi_{lS}^{n+1})$ as follows

$$\frac{\phi_0 N_M^{n+1} - \phi_0 N_M^{n+1/2}}{\tau} + A\chi_{lM}^{n+1} = f_M^{n+1}, \tag{17a}$$

$$N_M^{n+1} = S_l^{n+1}\chi_{lM}^{n+1} + R(1 - S_l^{n+1}). \tag{17b}$$

Here (17b) provides the definition of $N_M^{n+1}$ needed in (17a). The two unknowns in (17a) are $S_l^{n+1}$ and $\chi_{lM}^{n+1}$; these are connected to each other via (8) and (4)

$$\min(\chi_{lM}^{max,0}(x) + \alpha(x)\chi_{lS}^{n+1} - \chi_{lM}^{n+1}, 1 - S_l^{n+1}) = 0, \tag{17c}$$

with the dependence on $\chi_{lS}^{n+1}$ which is defined in turn by

$$\frac{\phi_0 N_S^{n+1} - \phi_0 N_S^{n+1/2}}{\tau} + A\chi_{lS}^{n+1} = 0, \tag{17d}$$

$$N_S^{n+1} = S_l^{n+1}\chi_{lS}^{n+1}. \tag{17e}$$

The system (17) is solved using Newton's method for $(S_l^{n+1}, \chi_{lM}^{n+1}, \chi_{lS}^{n+1})$, and the Jacobian of the system is a $3 \times 3$ sparse block matrix. Its form and particular pattern of sparsity depend on (17c). We refer to [9] for the details on the Jacobian in the one component case.

Note that in (17) we maintain full consistency of mass conservation between the time steps (up to the tolerance of nonlinear solver), as well as consistency of thermodynamic constraints.

### *3.4.2 Variant (SI): semi-implicit*

The semi-implicit variant differs from (17) in the treatment of $\chi_{lS}$ in (17c). We time-lag $\chi_{lS}$ and remove the two-way coupling between the methane transport and salinity transport. Methane transport in this model is governed by

$$\frac{\widehat{\phi_0 N_M^{n+1}} - \phi_0 N_M^{n+1/2}}{\tau} + A\widehat{\chi_{lM}^{n+1}} = f_M^{n+1}, \tag{18a}$$

$$\widehat{N_M^{n+1}} = \widehat{S_l^{n+1}}\,\widehat{\chi_{lM}^{n+1}} + R(1 - \widehat{S_l^{n+1}}). \tag{18b}$$

$$\min(\chi_{lM}^{max,0}(x) + \alpha(x)\widehat{\chi_{lS}^{n}} - \widehat{\chi_{lM}^{n+1}}, 1 - \widehat{S_l^{n+1}}) = 0. \tag{18c}$$

so that these equations are solved for $(\widehat{S_l^{n+1}}, \widehat{\chi_{lM}^{n+1}})$ using Newton's method. The Jacobian of the system is a $2 \times 2$ sparse block matrix.

Knowing $\widehat{S_l^{n+1}}$ we can solve the system for $\widehat{\chi_{lS}^{n+1}}$ which is linear

$$\frac{\widehat{\phi_0 N_S^{n+1}} - \phi_0 N_S^{n+1/2}}{\tau} + A\widehat{\chi_{lS}^{n+1}} = 0, \tag{18d}$$

$$\widehat{N_S^{n+1}} = \widehat{S_l^{n+1}}\,\widehat{\chi_{lS}^{n+1}}. \tag{18e}$$

While the mass conservation between the time steps is enforced in this variant, there is potential inconsistency in thermodynamic constraints introduced by the time-lagging in (18c). To correct this, we follow up with the two-variable local flash solver which corrects the saturations and solubilities while keeping ($\widehat{N_M^{n+1}}$, and $\widehat{N_S^{n+1}}$) fixed.

### *3.4.3 Variant (SEQ): sequential*

The sequential variant is the simplest to implement and one can easily adapt an existing advection-diffusion code. The advantage of this variant is that each of the global algebraic systems is linear. The disdvantage is that the phase behavior is not fully coupled to the transport dynamics, and fine time-stepping may be needed to ensure accuracy.

The SEQ variant time-lags the saturation variable in the methane and salinity transport equations

$$\frac{\phi_0 \widetilde{S_l^n} \widetilde{\chi_{lM}^{n+1,*}} - \phi_0 N_M^{n+1/2}}{\tau} + A\widetilde{\chi_{lM}^{n+1,*}} = f_M^{n+1} - \frac{\phi R(1-\widetilde{S_l^n})}{\tau}, \tag{19a}$$

$$\frac{\phi_0 \widetilde{S_l^n} \widetilde{\chi_{lS}^{n+1,*}} - \phi_0 N_S^{n+1/2}}{\tau} + A\widetilde{\chi_{lS}^{n+1,*}} = 0. \tag{19b}$$

Note that the phase constraint is not imposed in (19), and that the equations are not coupled. We solve them for the temporary unknowns $\widetilde{\chi_{lM}^{n+1,*}}, \widetilde{\chi_{lS}^{n+1,*}}$, and next we recalculate the mass concentrations corresponding to the new solubilities from (18b) and (18e)

$$\widetilde{N_M^{n+1}} = \widetilde{S_l^n}\widetilde{\chi_{lM}^{n+1,*}} + R(1-\widetilde{S_l^n}). \tag{20}$$

$$\widetilde{N_S^{n+1}} = \widetilde{S_l^n}\widetilde{\chi_{lS}^{n+1,*}}. \tag{21}$$

To keep these consistent with (8), we invoke the nonlinear two variable flash solver. Its input are the mass concentrations $\widetilde{N_M^{n+1}}, \widetilde{N_S^{n+1}}$, and its output are the final new values of solubilities $\widetilde{\chi_{lM}^{n+1}}, \widetilde{\chi_{lS}^{n+1}}$, and saturations $\widetilde{S_l^{n+1}}$ which satisfy the discrete version of (8) plus the mass concentration definitions

$$\min(\chi_{lM}^{max,0}(x) + \alpha(x)\widetilde{\chi_{lS}^{n+1}} - \widetilde{\chi_{lM}^{n+1}}, 1 - \widetilde{S_l^{n+1}}) = 0. \tag{22}$$

$$\widetilde{N_M^{n+1}} = \widetilde{S_l^{n+1}}\widetilde{\chi_{lM}^{n+1}} + R(1-\widetilde{S_l^{n+1}}). \tag{23}$$

$$\widetilde{N_S^{n+1}} = \widetilde{S_l^{n+1}}\widetilde{\chi_{lS}^{n+1}}. \tag{24}$$

The flash solver for (23)-(24) and (22) provides the consistency between the mass-related variables and thermodynamic constraints. However, the mass conservation between time steps is not strictly enforced due to time-lagging.

## 4 Comparison of time stepping variants

In this section we evaluate the accuracy, robustness and computational complexity of the proposed I, SI, and SEQ variants of hydrate models using realistic scenarios of methane hydrate formation in typical sediments. We also give details on what time steps appear reasonable, and how to choose discretization parameters.

In oil-gas reservoir simulation the fully implicit algorithms implement directly backward Euler formula, and are usually the most accurate, but also most complex to implement. In turn, sequential and semi-implicit variants are typically less accurate but, at least in principle, they have smaller computational complexity per time step, and are easier to implement than the fully implicit algorithms. Typically, the results of non-implicit schemes converge to those of fully implicit models as $\tau \to 0$. In fact, non-implicit variants may require small $\tau$ in in order to resolve, e.g. complicated phase equilibria, heterogeneity, or complex well behavior; the use of small $\tau$ somewhat erases the benefits of small computational cost per time step. The non-implicit variants may still have advantages in the easiness of implementation.

The computational experiments we set up to test the variants I, SI, and SEQ are built from the following base case similar to those in [18] for the methane hydrate and salinity conditions in Ulleung Basin.

We set $\Omega = (0, L)$ with $L = 159$m, and use uniform porosity $\phi = 0.5$. We vary $q$ from large $q = 0.1$m/yr for which advection dominates, to the case where diffusion is dominant and $q \leq 0.001$m/yr. We assume that advection and diffusion provide the only transport mechanisms and that $f_M = 0 = f_S$. For thermodynamics we use the reduced model (4) and [NCC-M] constraint is implemented with (8). Unless otherwise specified, we use the data $\chi^0_{max}(x)$ and $\alpha(x)$ calibrated for Ulleung Basin and shown in Fig. 6, with the same boundary and initial conditions. We use zero initial conidtions for methane, and an initial linear distribution of salinities between the boundary conditions $\chi^0_{lS}$ and $\chi^M_{lS}$. We run simulations until $T = 10^5$yr $= 100$Kyr, or until $S_h$ reaches the unphysical values close to 1.

Discretization parameters are chosen as follows. We use $N_x = 100$ with $h = 1.59$ in the base case. The time step is subject to the CFL constraint (15). In particular for $q = 0.01$ the largest time step $\tau_{CFL} \approx 78$yr.

For illustration of the base case in Fig. 2 we show the evolution of $S_h$ and $\chi_{lS}$ for the case $q = 0.01$m/yr, with small $\tau = 1$yr. In this case of strong advective flux the hydrate forms quickly and fills up the domain. These results are similar to those in [18] and more generally to the test cases in [14]. The evolution of salinity shows that there is a boundary layer close to the outflow which forms around $T = 10K$ and remains unchanged afterwards.

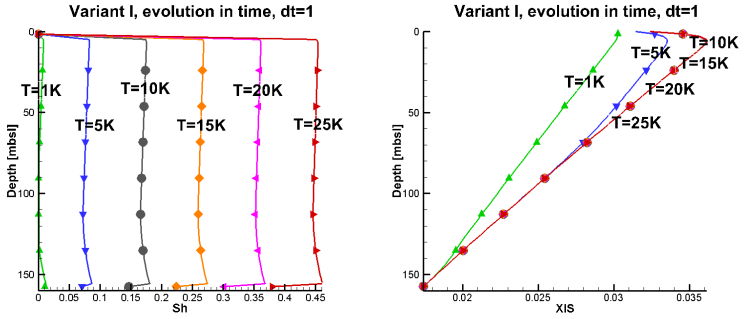


**Fig. 2** Evolution of hydrate saturation and of salinity for the base case. Left: plot of $S_h$, right: plot of $\chi_{lS}$. Variable $\chi_{lM}$ equals $\chi_{lM}^{max}$ at these times and is not shown.

| $\tau$ | SEQ | SI | I | $\tau$ | SEQ | SI | I |
|---|---|---|---|---|---|---|---|
| | $T = 10K$ | | | | $T = 25K$ | | |
| 78 | 0.177208 | 0.182844 | 0.182844 | 78 | 0.456162 | 0.463925 | 0.463925 |
| 70 | 0.176441 | 0.181803 | 0.181803 | 70 | 0.456803 | 0.464271 | 0.464271 |
| 50 | 0.176834 | 0.181267 | 0.181267 | 50 | 0.45644 | 0.462797 | 0.462797 |
| 25 | 0.177841 | 0.180908 | 0.180908 | 25 | 0.457708 | 0.462438 | 0.462438 |
| 10 | 0.178834 | 0.180736 | 0.180736 | 10 | 0.458886 | 0.462266 | 0.462266 |
| 5 | 0.179238 | 0.180688 | 0.180688 | 5 | 0.459731 | 0.462218 | 0.462218 |
| 1 | 0.180183 | 0.180651 | 0.180651 | 1 | 0.460878 | 0.462181 | 0.462181 |

**Table 2** Maximum hydrate saturation $S_h$ obtained with different model variants and time steps at $T = 10K$ and $T = 25K$, all parameters as in base case

### 4.1 Accuracy of the time-stepping variants and choice of time step

Here we study the sensitivity to $\tau$ which can guide its choice. In general, one wants to use small enough $\tau$ obeying the upper bound (15) and such that its further decrease does not have much influence. However, small $\tau$ means large number $\frac{T}{\tau}$ of time steps; this is significant in hydrate basin simulations since $\frac{T}{\tau}$ may be easily $10^4$ or more. Further, as suggested by our experience from oil-gas reservoir simulations [20,30,15], we expect that for small $\tau$ the results of the three variants I, SI, SEQ are very similar, and that for large $\tau$ they differ.

In Fig. 3 we present the plots of $S_h$ obtained for different $\tau$. Quantitative information supporting these observations is included in Tab. 2. (We do not present details concerning the evolution of $\chi_{lS}$ since the results differ by less than 0.01% in each case.) We notice that the results corresponding to $\tau = 1$ and the variants I, SI, and SEQ are essentially indistinguishable; this degree of closeness is more than expected. In addition, the results corresponding to the largest advection step $\tau = 78$ and to the variants I, SI and SEQ are close to each other as well; they tend to overpredict those for $\tau = 1$.

In addition, we see that the model SEQ is potentially the most sensitive of all three to $\tau$ close to the boundaries and in areas with larger methane gradients. (This suggests the need for adaptive gridding). In addition, as $\tau$

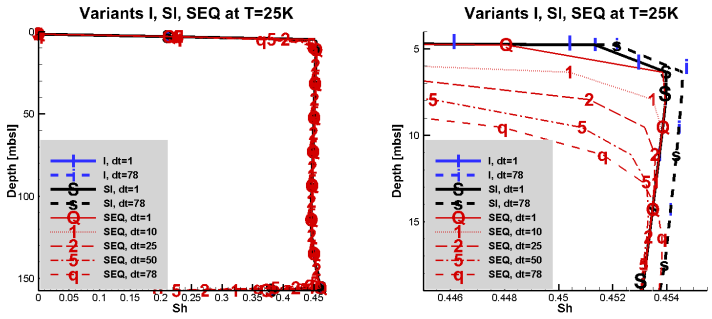


**Fig. 3** Plots of $S_h$ for different time steps $\tau$ (denoted on figure by $dt$), and different time-stepping variants I, SI, SEQ. Left: plots over full range of depth and $s_h$ are essentially indistinguishable. Right: zoomed in plot shows small sensitivity to the choice of time step and of the model variant.

| $\tau$ | SEQ | | SI | | I | |
|---|---|---|---|---|---|---|
| | $S_h^{crit}$ | $N_{it}$ | $S_h^{crit}$ | $N_{it}$ | $S_h^{crit}$ | $N_{it}$ |
| 78 | 0.75833 | - | 0.767473 | - | 0.773341 | - |
| 70 | 0.772449 | - | 0.782752 | - | 0.781435 | - |
| 50 | 0.806955 | - | 0.817198 | - | 0.817198 | - |
| 25 | 0.873396 | - | 0.880766 | - | 0.880766 | - |
| 10 | 0.925712 | 2 | 0.932267 | 2 | 0.932267 | 3 |
| 5 | 0.926744 | 2 | 0.93222 | 2 | 0.93222 | 3 |

**Table 3** Robustness of nonlinear solvers depending on variant and time step for simulations of base case between $T = 25K$ and $T = 50K$. We report the critical value $S_h^{crit}$ obtained before the solver fails, and on the number $N_{it}$ of iterations. $N_{it}$ denotes the number of flash iterations for SEQ model, and the number of global Newton iterations for the SI and I models. When $N_{it}$ is denoted by "-", this means the solver did not complete.

decreases, the results tend to converge to the value for $\tau = 1$. Further decrease of $\tau$ (not shown here) does not influence the solution much, thus $\tau = 1$ appears as the smallest sensible choice for this $N_x$.

## 4.2 Robustness and efficiency of the variants

Above we established that the simulated hydrate saturation values do not seem to significantly depend on the time step $\tau$ or on the variant of time stepping. Next we consider the robustness of the variants and in particular, how they handle difficult physical circumstances such as when $S_h$ is large due to large advective fluxes.

In Tab. 3 we report on the performance of the nonlinear solver, tested intentionally without any fine-tuning such as line-search. We see that between $T = 25K$ and $T = 50K$ all variants I, SI, SEQ struggle when $\tau \geq 25$. The model I appears somewhat more robust than the other two and it can simulate the hydrate evolution up to higher values.

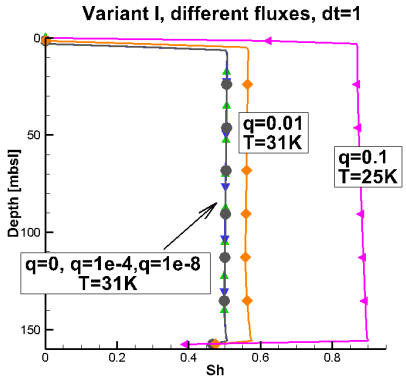


**Fig. 4** Hydrate saturation at $T = 31K$ when different advective fluxes are assumed. For $q = 0.1$ for which high saturation is attained already at $T = 25K$ we do not show the plot at $T = 31K$.

| $q$ | $T_I$ | $T_{SI}$ | $T_{SEQ}$ |
|---|---|---|---|
| 0.1 | 13917 | 13917 | 13972 |
| 0.01 | 27014 | 27014 | 27091 |
| 0.005 | 28629 | 28629 | 28691 |
| 0.0001 | 30568 | 30568 | 30587 |
| 1e-08 | 30614 | 30614 | 30624 |

**Table 4** The time when $\max S_h \approx 0.5$ for each variant depending on $q$. Here we use $\tau = 1$ applied to the base case.

*Dependence of the results on q.* Next we consider the advection-dominated case down to diffusive case $q = 0$. In Fig. 4 we present the plots of hydrate saturations at $T = 31K$ for different fluxes $q$. In addition, in Tab. 4 we report the time $T_I$ when the computational model I predicts that $\max_x S_h(x, T_I) \approx 0.5$. We also report the values $T_{SI}$ and $T_{SEQ}$ also for the variants SI and SEQ. We see that I and SI report essentially the same values. In fact, a close inspection reveals that the model results differ in less than 0.001% between I and SI for the time steps we used in our implementation. This experiment shows again the robustness of all variants with respect to $q$, with a slight advantage of the implicit variants.

*Computational time.* In Tab. 5 we report the wall clock time for our MATLAB implementation. In order to compare the solvers on equal footing, no special vectorization was implemented.

In general one expects that for the same time step $\tau$ the SEQ model is faster than SI and I, since SEQ only uses global linear solvers and local nonlinear flash routines. However, we see that all solvers require similar amounts of computational time, with a slight advantage of model SI. This may be due to the lack of vectorization applied in local flash routines, while the global linear solvers are naturally vectorized in MATLAB. In addition, the SEQ solver computes more local variables than SI and I.

| dt | $T^w_{\mathrm{SEQ}}$ | $T^w_{\mathrm{SI}}$ | $T^w_{\mathrm{I}}$ |
|---|---|---|---|
| 1 | 591.801 | 439.806 | 441.394 |
| 10 | 60.2528 | 44.0688 | 47.6352 |
| 50 | 11.8322 | 8.81442 | 9.63327 |
| 78 | 7.55206 | 5.655 | 6.08011 |

**Table 5** Comparison of computational wall clock time $T^w[s]$ for the three model variants and different time steps, for the base case and $T = 25K$

| $N_x$ | $h$ | $\tau$ | $\max S_h$ | Wall-clock time |
|---|---|---|---|---|
| 10 | 15.9 | 10 | 0.453079 | 5.6533 |
| 25 | 6.36 | 4 | 0.455525 | 32.644 |
| 50 | 3.18 | 2 | 0.459280 | 121.411 |
| 100 | 1.59 | 1 | 0.462181 | 489.101 |
| 200 | 0.795 | 0.5 | 0.465253 | 2301.53 |

**Table 6** Accuracy and complexity of the computational model depending on $N_x$, with the time step $\tau$ adjusted to vary linearly with $h$. As the quantity of interest depending on $N_x$ we show the saturation values at $T = 25K$. This table complements the plots in Fig. 5

The efficiency of the solvers may be very different in 2d or 3d simulations, and we intend to report on these in the future.

Since with uniform $\tau$ the total computational time scales proportionally to the number of time steps, the choice of $\tau$ balances the desired accuracy and computational time. For the case considered here it seems that the time step $\tau = 10$ may be the best practical choice.

## 5 Sensitivity to physical and coputational parameters

For a computational model it is crucial to determine what discretization parameters one should use for a given model. In addition, it is important to investigate the sensitivity of the model to the data on $\alpha(x)$ in (4).

*Discretization parameters.* As the discretization parameters $h, \tau \to 0$ and the numbers of cells $N_x = \frac{L}{h}$ and time steps increase, it is expected that the numerical solutions of a PDE model converge to the analytical ones in an appropriate sense dictated by the theoretical numerical analysis. The convergence studies for the purely diffusive one component case of (3) in [9] suggest to vary $\tau$ wit $h$ either linearly or faster, and to consider various metrics of convergence in appropriate functional spaces. For the present case with significant advection $q$ and variable salinity, we expect the rates to be inferior of the approximate $O(h + \tau)$ rates observed in [9]. The theoretical analysis is underway and will be presented elsewhere.

Here we choose $\tau = O(h)$ and the implicit model; in Fig. 5 and Tab. 6 we present the evidence which confirms that as $h$ decreases, the results seem to converge, but it is obvious that the convergence in saturations is quite rough, as observed in [22].

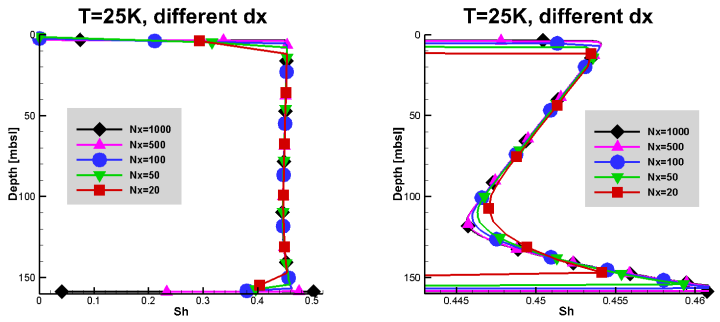


**Fig. 5** Hydrate saturation for different $N_x$ and $h$ denoted by dx. See Tab. 6 for the related quantitative information extracted from the simulations

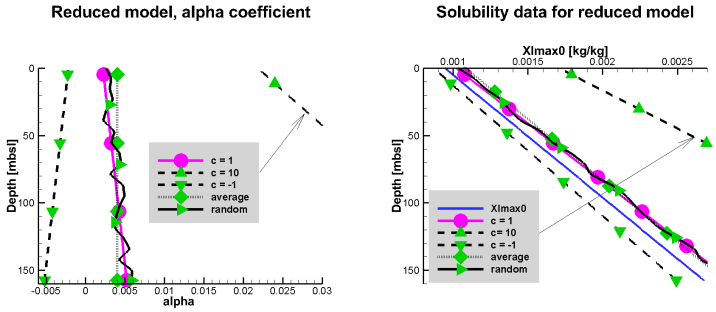


**Fig. 6** Parameter $\alpha(x)$ as a function of depth used in Sec. 5 (left) and the corresponding $\chi_{lM}^{max,0}(x)$ computed from (4) and assuming $\chi_{LS} \approx \chi_{lS}^{sw}$ (right). On right the plot of $\chi_{lM}^{max,0}(x)$ is also shown. The base case from Ulleung Basin [18] in both plots is denoted with circles. The other cases correspond to $c = -1$, $c = 10$, the average of $\alpha(x)$, and to a randomly perturbed $\alpha(x)$. The plots for $c = 10$ are out of range and are not fully included.

Overall, the convergence results presented seem to suggest that $N_x = 100$ or $N_x = 50$ corresponding to spatial $h \approx 1$m and $\tau \approx 1$yr are a good choice balancing the computational time and accuracy.

*Sensitivity to the parameters of the reduced model* (4). There is large uncertainty as to what $\chi_{lM}^{max}$ one should use. In particular, there may be an error associated with the look-up table process of finding $\alpha$ described in [18] and due to the lack of information on salinity. More broadly, in a comprehensive model $\chi_{lM}^{max}$ depends on the unknown pressure and temperature values, and possibly rock type, thus further variability and uncertainty of $\alpha(x)$ should be expected.

We set up therefore test cases to assess this sensitivity. We dub the values of $\alpha(x)$ obtained for Ulleung Basin in [18] the "true" $\alpha_{\text{true}}(x)$. Next we simulate the hydrate formation with $\alpha(x) = c\alpha_{\text{true}}(x)$ with $c = 1, c = 10$ and $c = -1$. Furthermore, we consider a constant value equal to the average of the

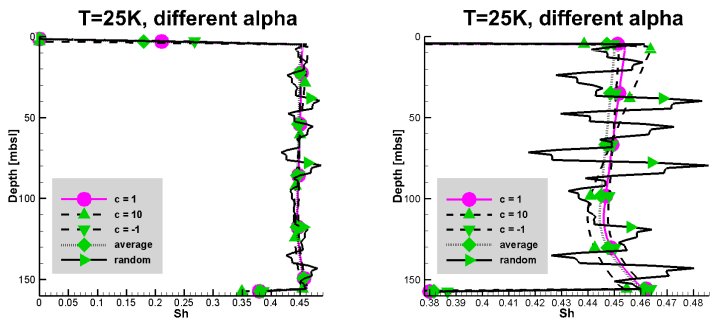


**Fig. 7** Hydrate saturation for different coefficients $\alpha$. The figure on the right is a zoomed in version of that on the left.

true $\alpha(x) = \frac{1}{|\Omega|}\int_\Omega \alpha_{\text{true}}(x)dx$, and another $\alpha(x)$ which randomly perturbes $\alpha_{\text{true}}(x)$. The different cases of $\alpha$ are shown in Fig. 6, with the corespnding $\chi_{lM}^{max}$ which we calculated, for illustration purposes, assuming $\chi_{lS} = \chi_{lS}^{sw}$. In Fig. 7 we show the profiles of $S_h$ at $T = 25K$ coresponding to the different $\alpha(x)$.

Comparing the hydrate saturation for $c = -1$ and $c = 10$ shown in Fig. 7 to the base case with $c = 1$ we see that since $\chi_{lM}^{max}$ is significantly higher when $c = 10$, somewhat less hydrate forms. On the other hand, a randomly pertubed $\alpha(x)$ gives $\chi_{lM}^{max}$ with large local variation, and this is reflected in the corresponding hydrate saturation. This significant sensitivity appears to be of qualitative nature, and requires further studies.

## 6 Conclusions

In this paper we describe the details of the discretization and implementation of a reduced methane hydrate model with variable salinity and significant advection, originally proposed in [18]. We carry out several convergence and parameter studies that show that the model is robust and computationally sound. Studies of this type were not available either for the simplified or the comprehensive hydrate models from literature, but are necessary to guide the implementation and further theoretical developments.

Several time stepping variants: implicit I, semi-implicit SI, and sequential SEQ, were tested and compared. We found, somewhat surprisingly, that the I and SI variants give almost identical results; this may be explained by only a mild dependence of the model on the salinity variable whose treatment differs in I and SI. Furthermore, in the current implementation and 1d test cases there is no significant advantage in one variant over the others as concerns accuracy, robustness, or efficiency. Still, the I model appears as expected somewhat most robust, while SEQ is the easiest to implement by modifying standard advection-diffusion solvers. We also demonstrated the apparent convergence of the solutions when $h, \tau \to 0$, and determined practical choices of

$h, \tau$. In addition, there is apparent need for grid and model refinement near the boundaries.

Furthermore, we demonstrated the small sensitivity of the reduced thermodynamics model proposed in [18] to the particular value of the coefficient $\alpha$ as long as it is qualitatively close to the one from data and monotone. However, a randomly perturbed and nonmonotone $\alpha$ reveals large sensitivity, and we plan to investigate the reasons further.

Our future work includes theoretical and practical studies of the model convergence as well as its efficiency. There is further need to realistic data and thermodynamics models, and extensions to more complex physical problems.

## References


1. Center for Hydrate Research Software CSMHYD and CSMGem. URL http://hydrates.mines.edu/CHR/Software.html. Accessed April 9, 2015
2. Chen, Z., Khlopina, N.L.: Degenerate two-phase incompressible flow problems. i. regularization and numerical results. Commun. Appl. Anal. **5**(3), 319–334 (2001)
3. Class, H., Helmig, R.: Numerical simulation of non-isothermal ultiphase multicomponent processes in porous media 2. applications for the injection of steam and air. Advances in Water Resources **25**, 533–550 (2002)
4. Coats, K.H., Thomas, L.K., Pierson, R.G.: Compositional and black oil reservoir simulator. In: the 13th SPE symposium on reservoir simulation. San Antonio, Texas (1995)
5. Daigle, H., Dugan, B.: Capillary controls on methane hydrate distribution and fracturing in advective systems. Geochemistry, Geophysics, Geosystems **12**(1) (2011)
6. Dawson, C.N.: Godunov-mixed methods for advection-diffusion equations in multidimensions. SIAM J. Numer. Anal. **30**, 1315–1332 (1993)
7. Dawson, C.N., Wheeler, M.F.: Time-splitting methods for advection-diffusion-reaction equations arising in contaminant transport. In: J. R. E. O'Malley (ed.) Proceedings of the second International Conference on Industrial and Applied Mathematics, ICIAM'91, pp. 71–82. SIAM, Philadelphia (1991)
8. Gharbia, I.B., Jaffre, J.: Gas phase appearance and disappearance as a problem with complementarity constraints. Mathematics and Computers in Simulation **to appear** (2013). DOI http://dx.doi.org/10.1016/j.matcom.2013.04.021. URL http://www.sciencedirect.com/science/article/pii/S0378475413001924
9. Gibson, N.L., Medina, F.P., Peszynska, M., Showalter, R.E.: Evolution of phase transitions in methane hydrate. Journal of Mathematical Analysis and Applications **409**(2), 816 – 833 (2014). DOI http://dx.doi.org/10.1016/j.jmaa.2013.07.023. URL http://www.sciencedirect.com/science/article/pii/S0022247X13006628
10. Helmig, R.: Multiphase flow and transport processes in the Subsurface. Springer (1997)
11. Ito, K., Kunisch, K.: Semi-smooth Newton methods for variational inequalities of the first kind. M2AN Math. Model. Numer. Anal. **37**(1), 41–62 (2003). DOI 10.1051/m2an:2003021
12. Lake, L.W.: Enhanced oil recovery. Prentice Hall (1989)
13. LeVeque, R.J.: Finite difference methods for ordinary and partial differential equations. Society for Industrial and Applied Mathematics (SIAM), Philadelphia, PA (2007). Steady-state and time-dependent problems
14. Liu, X., Flemings, P.B.: Dynamic multiphase flow model of hydrate formation in marine sediments. Journal of Geophysical Research **112**, B03,101 (2008)
15. Lu, Q., Peszyńska, M., Wheeler, M.F.: A parallel multi-block black-oil model in multimodel implementation. SPE Journal **7**(3), 278–287 (2002). SPE 79535
16. Nimblett, J., Ruppel, C.: Permeability evolution during the formation of gas hydratees in marine sediments. Journal of Geophysical Research **108**, B9, 2420 (2003)
17. Peaceman, D.W.: Fundamentals of numerical reservoir simulation, first edn. Elsevier Scientfic Publishing Company, Amsterdam-Oxford-New York (1977)

18. Peszynska, M., Hong, W.L., Torres, M., Kim, J.H.: Methane hydrate formation in ulleung basin under conditions of variable salinity i. reduced model and experiments. Submitted
19. Peszyńska, M., Jenkins, E., Wheeler, M.F.: Boundary conditions for fully implicit two-phase flow model. In: X. Feng, T.P. Schulze (eds.) Recent Advances in Numerical Methods for Partial Differential Equations and Applications, *Contemporary Mathematics Series*, vol. 306, pp. 85–106. American Mathematical Society (2002)
20. Peszyńska, M., Lu, Q., Wheeler, M.F.: Multiphysics coupling of codes. In: L.R. Bentley, J.F. Sykes, C.A. Brebbia, W.G. Gray, G.F. Pinder (eds.) Computational Methods in Water Resources, pp. 175–182. A. A. Balkema (2000)
21. Peszynska, M., Showalter, R., Webster, J.: Advection of methane in the hydrate zone: Model, analysis and examples. Mathematical Methods in the Applied Sciences **accepted** (2014). URL http://www.math.oregonstate.edu/ mpesz/documents/publications/PSW.pdf
22. Peszyńska, M., Torres, M., Tréhu, A.: Adaptive modeling of methane hydrates. In: International Conference on Computational Science, ICCS 2010, Procedia Computer Science, available online via www.elsevier.com/locate/procedia and www.sciencdirect.com, vol. 1, pp. 709–717 (2010)
23. Rempel, A.W.: Hydromechanical processes in freezing soils. Vadose Zone Journal **11**(4) (2012). DOI 10.2136/vzj2012.0045. URL http://vzj.geoscienceworld.org/content/11/4/vzj2012.0045.abstract
24. Russell, T.F., Wheeler, M.F.: Finite element and finite difference methods for continuous flows in porous media. In: R.E. Ewing (ed.) The Mathematics of Reservoir Simulation, pp. 35–106. SIAM, Philadelphia (1983)
25. Sloan, E., Koh, C.A.: Clathrate Hydrates of Natural Gases, third edn. CRC Press (2008)
26. Torres, M., Wallmann, K., Tréhu, A., Bohrmann, G., Borowski, W., Tomaru, H.: Gas hydrate growth, methane transport, and chloride enrichment at the southern summit of Hydrate Ridge, Cascadia margin off Oregon. Earth and Planetary Science Letters **226**(1-2), 225 – 241 (2004). DOI DOI: 10.1016/j.epsl.2004.07.029
27. Trangenstein, J.A., Bell, J.B.: Mathematical structure of the black-oil model for petroleum reservoir simulation. SIAM J. Appl. Math. **49**(3), 749–783 (1989)
28. Ulbrich, M.: Semismooth Newton methods for variational inequalities and constrained optimization problems in function spaces, *MOS-SIAM Series on Optimization*, vol. 11. Society for Industrial and Applied Mathematics (SIAM), Philadelphia, PA (2011). DOI 10.1137/1.9781611970692. URL http://dx.doi.org/10.1137/1.9781611970692
29. Wheeler, M.F., Dawson, C.N.: An operator-splitting method for advection-diffusion-reaction problems. In: J.R. Whiteman (ed.) The Mathematics of Finite Elements and Applications VI, pp. 463–382. Academic Press, London (1987)
30. Wheeler, M.F., Peszyńska, M.: Computational engineering and science methodologies for modeling and simulation of subsurface applications. Advances in Water Resources **25**(8-12), 1147–1173 (2002)
31. Wheeler, M.F., Wheeler, J.A., Peszyńska, M.: A distributed computing portal for coupling multi-physics and multiple domains in porous media. In: L.R. Bentley, J.F. Sykes, C.A. Brebbia, W.G. Gray, G.F. Pinder (eds.) Computational Methods in Water Resources, pp. 167–174. A. A. Balkema (2000)
32. Xu, W., Ruppel, C.: Predicting the occurence, distribution, and evolution of methane hydrate in porous marine sediments. Journal of Geophysical Research **104**, 5081–5095 (1999)
33. Zatsepina, O., Buffett, B.: Phase equilibrium of gas hydrate: Implications for the formation of hydrate in the deep sea floor. GEOPHYSICAL RESEARCH LETTERS **24**(13), 1567–1570 (1997). DOI 10.1029/97GL01599

**National Energy Technology Laboratory**

626 Cochrans Mill Road
P.O. Box 10940
Pittsburgh, PA 15236-0940

3610 Collins Ferry Road
P.O. Box 880
Morgantown, WV 26507-0880

13131 Dairy Ashford, Suite 225
Sugarland, TX 77478

1450 Queen Avenue SW
Albany, OR 97321-2198

2175 University Ave. South
Suite 201
Fairbanks, AK 99709

Visit the NETL website at:
www.netl.doe.gov

Customer Service:
1-800-553-7681